Analysis of translating mitoribosome reveals functional characteristics of translation in mitochondria of fungi

Yuzuru Itoh[1,2†], Andreas Naschberger[1†], Narges Mortezaei[1†], Johannes M. Herrmann[3] and Alexey Amunts[1,2*]

[1]Science for Life Laboratory, Department of Biochemistry and Biophysics, Stockholm University, 17165 Solna, Sweden

[2]Department of Medical Biochemistry and Biophysics, Karolinska Institutet, 17165 Solna, Sweden

[3]Cell Biology, University of Kaiserslautern, Erwin-Schrödinger-Straße 13, 67663 Kaiserslautern, Germany

† These authors contributed equally to this work.

* email: amunts@scilifelab.se

Abstract

Mitoribosomes are specialized protein synthesis machineries in mitochondria. However, how mRNA binds to its dedicated channel, and tRNA moves as the mitoribosomal subunit rotate with respect to each other is not understood. We report models of the translating fungal mitoribosome with mRNA, tRNA and nascent polypeptide, as well as an assembly intermediate. Mitochondria-specific rRNA and protein elements coordinate binding of nicotinamide adenine dinucleotide (NAD) in the central protuberance of the large subunit and the ATPase inhibitory factor 1 (IF_1) in the small subunit. The models of the active mitoribosome explain how mRNA binds through a dedicated protein platform on the small subunit, tRNA is translocated with the help of newly identified protein mL108, bridging it with L1 stalk on the large subunit, and nascent polypeptide paths through a newly shaped exit tunnel involving a series of structural rearrangements. An assembly intermediate is modeled with the maturation factor Atp25, providing insight in to the biogenesis of the mitoribosomal large subunit and translation regulation.

Introduction

Protein synthesis in mitochondria supports bioenergetics of eukaryotic cells and is executed by dedicated mitoribosomes. Electron cryo-microscopy (cryo-EM) has been instrumental in revealing the first structural snapshots of mitoribosomes. While for mammals the obtained models from human embryonic kidney cells (Amunts *et al*, 2015; Brown *et al*, 2014) are in agreement with those from porcine and bovine tissues (Greber *et al*, 2015; Greber *et al*, 2014), the structure of the mitoribosome from the yeast *Saccharomyces cerevisiae* displayed considerable specializations (Amunts *et al*, 2014; Desai *et al*, 2017). Particularly, it proposed a distinct composition and putative deviations in the functionally defining features of translation, including an expanded mRNA channel exit and rerouted polypeptide exit channel. Although the existing cryo-EM data is informative, the deviations of the mitoribosome from *S. cerevisiae* that lacks complex I are more likely species-specific and therefore cannot be considered as a prototypic example of fungi. In addition, the available models are incomplete due to the limited resolution. Therefore, in the absence of high-resolution structural information of the translating mitoribosome, key questions regarding mitochondrial translation remain open. To provide a representative reference for studying protein synthesis in the mitochondria of fungi, and to reveal how the mitoribosome functions in coordination with its translation partners, we determined structures of the translating mitoribosome from the representative fungal model organism *Neurospora crassa.*

N. crassa has been recognized as the organism used for answering a variety of fundamental biological questions in the field of mitochondrial translation, and low resolution reconstruction of the mitoribosome was reported (van der Sluis *et al*, 2015). Other contributions of this model organism include early characterization of the physicochemical properties of the mitoribosomes and the base composition of its rRNA (Kuntzel & Noll, 1967), the finding that mitoribosomal intactness requires a relatively high magnesium concentration (Kuntzel, 1969), studies showing radioactive amino acid incorporation into mitoribosome (Neupert *et al*, 1969), and the finding that Oxa1 facilitates integration of mitochondrially encoded proteins into the inner membrane (Nargang *et al*, 2002). Therefore, to provide a reference for the process of protein synthesis in mitochondria, we set out to investigate the functional translation apparatus from the model organism *N. crassa.*

Results and Discussion

Structure determination

In order to characterize a representative functional mitoribosome, the *N. crassa* mycelia of the strain K5-15-23-1 overexpressing the protein Oxa1 (Nargang *et al.*, 2002) were grown aerobically and translation was stalled using chloramphenicol prior to harvesting. The mycelia were dried, lysed with mortar and pestle, and the mitoribosomes were purified as described previously (Aibara *et al*, 2018), and subjected to cryo-EM analysis. The cryo-EM consensus map was obtained from 131,806 particles at overall resolution of 2.83 Å (Appendix Fig S1 and Appendix Table S1).

The 3D classification resulted in two reconstructions of the mitoribosome corresponding to the rotated and non-rotated states (Appendix Fig S1). After subtracting the mitoribosome signals outside the tRNA binding sites, followed by focused 3D classifications, we obtained three distinct

classes of mitoribosomes with a tRNA occupying P-site (P/P), E-site (E/E), and in the hybrid P/E state, at the overall resolutions of 3.05, 3.10, and 2.99 Å, respectively (Appendix Fig S1). In the P/P and P/E tRNA states, we detected and modeled co-purified native mitochondrial mRNA, and the density corresponding to the nascent polypeptide was identified in the P/P tRNA state.

To further improve the local resolution, focused masked refinements were performed using the masks for the large subunit (mtLSU) core, central protuberance (CP), L1 stalk, uL10m region, the small subunit (mtSSU) head, body and tail (Appendix Figs S2 to S5). Consequently, the resolution was improved to ~2.50-3.40 Å throughout most of the regions. The quality of the maps allowed building the most complete available model, including identification of five proteins previously missed in the yeast structure: uL1m, uL10m, uL11m, mL53, and mL54; two newly identified mitoribosomal proteins: mL108 and the ATP synthase inhibitory factor 1 (IF_1); and 60 proteins with higher completeness, as well as the rRNAs (Fig 1A, Fig EV1 and Appendix Figs S6 to S9).

In addition, we noted that mitoribosomes from actively growing *N. crassa* mycelia contain a pool of free mtLSU (Appendix Fig S5), which resembles the profile of the assembly intermediate reported from the mitochondria of human embryonic kidney cells (Brown *et al*, 2017). Unlike the mtLSU in the intact mitoribosome, this population is missing the density for bL9m, but has an extra factor Atp25 bound to uL14m, and a poor density at the interface consistent with unfolded mt-rRNA. The quality of the structural data allowed the analysis of the differences with the mature mtLSU, and to propose a putative regulatory mechanism.

Overall structure and new features

The fungal mitoribosome consists of 78 different proteins, 23S and 16S rRNAs (Fig 1, Appendix Figs S6 to S9 and Appendix Tables S2 and S3). The proteins mS42 and IF_1 are found in two copies as homodimers. 48 bacterial orthologs are extended, and 30 proteins are mitochondria-specific. For the rRNA, we modeled 16 expansion segments (ES), 15 of which are in the mtLSU (Appendix Figs S6 to S8), and several other rRNA regions have been reduced. The deletion in the mtDNA genome are not correlated with a specific functional feature or attributed to selective loss/gain of activity, but rather reflect a general reductive phase in the mitochondrial genome (van der Sluis *et al.*, 2015). For the native mitochondrial tRNAs (P/P, P/E, E/E states) and mRNA, we modeled nucleotide sequences that fit the corresponding densities the best, because those densities represent a mixture of different tRNAs and mRNAs in mitochondria.

Some of the improvements in the model due to the high-resolution map are exemplified in Fig 1. Protein mS27, which was previously partially built as poly-Ala, has been identified directly from the density as a helical repeat protein consistent with mammalian counterparts. We named it accordingly mS27 (previously mS44) (Fig 1B, Appendix Fig S10 and Appendix Table S3). Another example is the protein mS29 that was reported as a GTPase involved in apoptosis, and mutations in the P-loop motif of the nucleotide binding pocket were suggested to impair this function (Kim *et al*, 2017). In the nucleotide pocket of mS29, which was previously modeled with guanosine diphosphate (GDP), we can see at the local resolution of 2.77 Å that the density for N2 purine ring atom is missing, and the correct assignment for the nucleotide is adenosine triphosphate

(ATP) (Fig 1B and Appendix Fig S11). This is further supported by the better resolved chemical environment formed by Leu150 of mS29, which would be incompatible with guanine since the O6 carbonyl of guanine imparts repulsive interaction with the backbone carbonyl of Leu150 (acceptor with acceptor), and the NH1 group of guanine forms a second repulsive interaction with the backbone NH group of Leu150 (donor with donor). Placing an ATP instead of GDP leads to more favorable interactions.

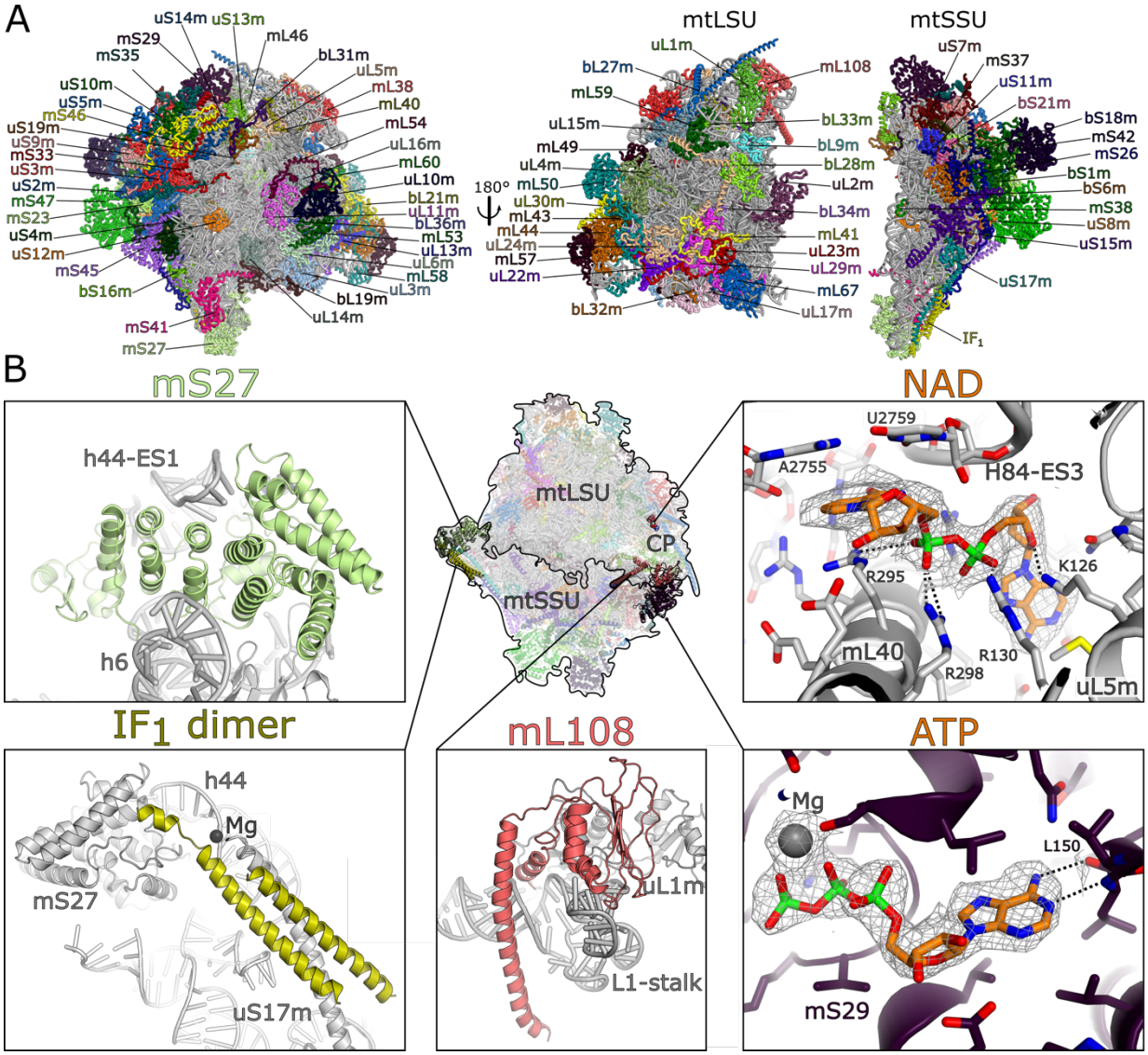

Figure 1. Structure of the fungal mitoribosome and new features. (A) Overall structure of the complete mitoribosome and its subunits with indicated mitoribosomal proteins. (B) Examples of newly identified features. Remodeled and reannotated mS27 interacts with h44-ES1. Newly identified mitoribosomal component IF_1 dimer bound to h44-ES1 and uS17m extension. NAD binding pocket in the CP formed by uL5m, mL40, and H84-ES3. Newly identified mitoribosomal component mL108 is located in the L1 stalk. Nucleotide binding pocket of mS29 bound with chemically favorable ATP shown with its density.

In the CP, we found an extra density in the pocket formed by mL40, uL5m, and rRNA H84-ES3 (Fig 1B). Based on the density, interactions and the abundance in mitochondria, we conclude that the it is the most likely to be NAD (Appendix Fig S12). Positively charged residues of mL40 and uL5m interact with the negatively charged NAD phosphates. The pyridine ring of the nicotinamide is held in place by π-stacking on the base pair of A2755 and U2759. Arg295 of mL40 forms π-stacking at the other side of the NAD pyridine. Therefore, NAD bridges the mitoribosomal proteins and the mt-rRNA at the core of CP. This implies regulatory function in the assembly of the mtLSU based on the local NAD level.

In the mtSSU tail, we found an extra density corresponding to helical structures of protein chains. The density (Fig EV1 and Fig EV2) and the mass-spectrometry data (Appendix Table S4) suggested that it is the natural inhibitor of the mitochondrial ATP synthase IF_1 bound as a homodimer (Fig 1B). In the ATP synthase, IF_1 functions through inserting its N-terminal part into the catalytically active F_1-ATPase, thereby blocking its rotational movement and subsequently the ATP hydrolase activity (Cabezon *et al*, 2003; Robinson *et al*, 2013). In our structure of the mitoribosome, IF_1 coiled-coil forms a helical bundle with the C-terminal extension of uS17m and also binds to mS27 and h44 rRNA (Fig 1B and Fig EV2). It is also bridged through a metal ion Mg^{2+}, coordinated by uS17m Q162 and the backbone phosphate of h44 A1745 (Fig EV2C). The topology of IF_1 homodimer is such that the C-terminus of each monomer points in the opposite direction: one towards the mtSSU body, and the other towards the solvent. Although the topology resembles that of the bovine IF_1 homodimer (Cabezon *et al*, 2001) (Fig EV2A), the dimerization region is shifted ~7 residues toward the N-terminus and is shorter by ~10 residues, suggesting it is less stable. In addition, against the sequence similarity with the yeast counterpart (Fig EV2B), we find differences in topology when compared with the X-ray crystal structure of the *S. cerevisiae* IF_1 monomer bound to the F_1-ATPase (Robinson *et al.*, 2013) (Fig EV2A). Particularly, the *S. cerevisiae* IF_1 has a short helix α1 followed by a longer helix α2, whereas in *N. crassa* the α1 counterpart region appears to be disordered, and α2 comprises two helices separated by 2 residues. The differences might also be affected by different binding partners (mitoribosome vs F_1-ATPase), reflecting the structural flexibility of IF_1. Since the C-terminal extension of uS17m stabilizing the IF_1 on the mitoribosome is specific to *N. crassa* (Fig EV2C) the feature of IF_1 binding might also be specific. Our structural analysis shows that h44 is expanded in this region of the mitoribosome, which would suggest that IF_1 has been acquired through the mechanism of 'structural patching' to stabilize the rapidly evolving growth (Petrov *et al*, 2019).

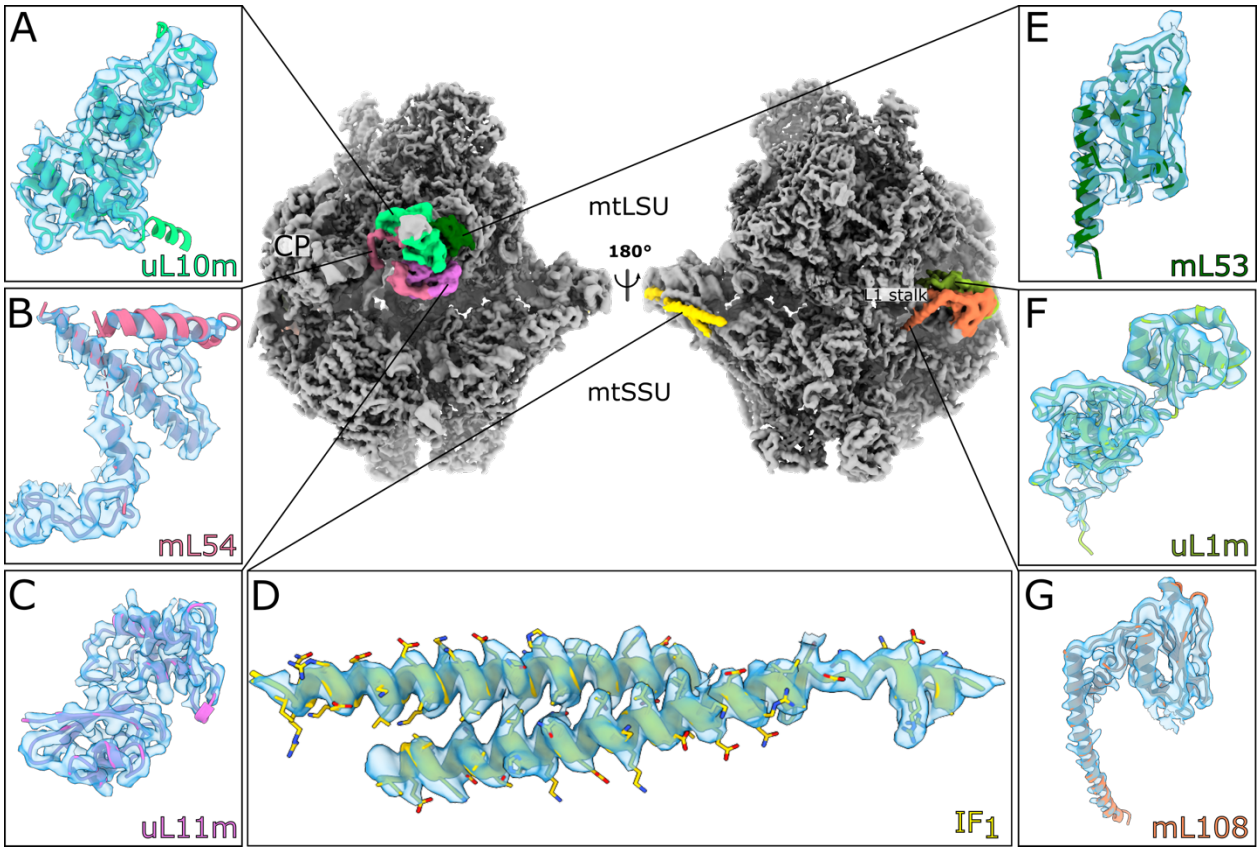

Figure EV1. Cryo-EM reconstruction and newly modelled proteins. Two views of a composite cryo-EM map with newly identified proteins colored. The close-up views show the newly modeled proteins with their corresponding density map: (A) uL10m. (B) mL54. (C) uL11m. (D) IF_1. (E) mL53. (F) uL1m. (G) mL108.

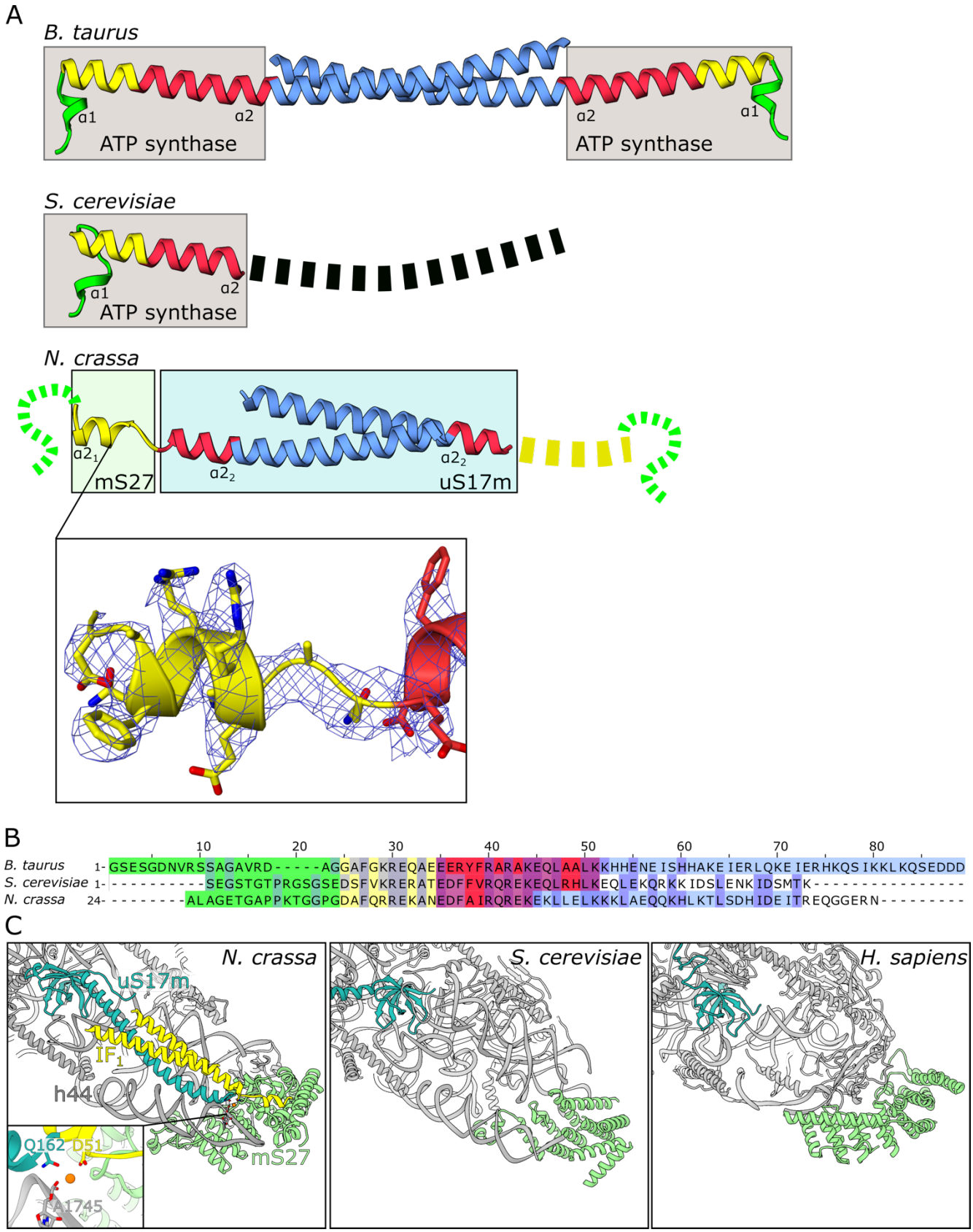
A
B. taurus
α1
α2
ATP synthase
α2
α1
ATP synthase
S. cerevisiae
α1
α2
ATP synthase
N. crassa
α2₁
mS27
α2₂
α2₂
uS17m
B
10
20
30
40
50
60
70
80
B. taurus 1- GSESGDNVRSSAGAVRD-----AGGAFGKREQAEEERYFRARAKEQLAALKKHHENEISHHAKEIERLQKEIERHKQSIKKLKQSEDDD
S. cerevisiae 1- ----------SEGSTGTPRGSGSEDSFVKRERATEDFFVRQREKEQLRHLKEQLEKQRKKIDSLENKIDSMTK----------
N. crassa 24- --------ALAGETGAPPKTGGPGDAFQRREKANEDFAIRQREKEKLLELKKKLAEQQKHLKTLSDHIDEITREQGGERN--------
C
N. crassa
uS17m
IF1
h44
mS27
Q162
D51
A1745
S. cerevisiae
H. sapiens

Figure EV2. IF_1 topology, structure, binding and conservation. (A) IF_1 structure is compared with those of *Bos taurus* (generated from PDB IDs: 1GMJ (Cabezon *et al.*, 2001) and 4TFS (Bason *et al*, 2014)) and *S. cerevisiae* (PDB ID: 3ZIA). Density map with model is shown to illustrate the quality of the data in this region. The mitoribosome and F_1-ATPase binding parts are indicated with boxes. For *N. crassa*, the disordered N-terminal region (residues 24-39), the short helix $\alpha2_1$ with a loop (residues 40-49), the longer helix $\alpha2_2$ outside the dimerization part (residues 50-58), and $\alpha2_2$ within the dimerization part (residues 59-88) are colored as green, yellow, red, and blue, respectively. Corresponding residues are colored accordingly in *B. taurus* and *S. cerevisiae*, where α1 is located in the N-terminal region and $\alpha2_1$ and $\alpha2_2$ are a continuous helix α2. (B) Structure-based sequence alignment, colored as in A. The mitochondria targeting sequence is included in the residue numbering for *N. crassa*. (C) Structure of the IF_1-binding site of *N. crassa* mtSSU and the corresponding regions from *S. cerevisiae* and *H. sapiens*. IF_1, uS17m, and mS27 are indicated. The IF_1 homodimer forms a helical bundle with the specific C-terminal extension of uS17m. The Mg-ion mediated bridge is shown in a zoom-in window.

The mechanism of mRNA binding involves a dedicated protein platform

Focused classifications on the tRNA binding sites yielded structures of three distinct classes with bound tRNA in P/P, P/E, E/E (Appendix Fig S1). The quality of the density allowed us to generate structural models of the mitoribosomal complexes with P/P and P/E tRNAs. The presence of tRNAs correlates with additional density lining the mRNA channel path, where a well resolved map allowed modeling of 11 nucleotides of the native mRNA (see Methods). The codon-anticodon base pairings are observed in the density of the P/P and P/E states (Fig 2). The decoding center is conserved, including the position of the bases A1803 (A1492 in *E. coli*), A1804 (A1493) and G756 (G530), as well as the curvature in mRNA around h28. In addition to the modeled mRNA nucleotides in the channel, bulky density extends upstream to the channel entry and downstream to its exit. Therefore, the map allows us to determine how mRNA binds to the mitoribosome and to trace its complete path.

The reference point to the channel entry is the universal site formed by uS3m, uS4m, and uS5m. Compared to the previously determined structures of the bacterial complex, mitochondrial mRNA is also bound by mitochondria-specific protein mS35. However, the density for the mRNA chain starts prior to the conventional entry. Particularly, following the density, we observe extended structure involving mitochondria-specific extensions of uS3m and uS5m that are held together at the mtSSU head by mS35 and mS46 (Fig 2A). This architecture is coupled to the mRNA terminus, thereby suggesting a potential platform for its loading on to the mitoribosome. The formed loading platform narrows the entry site considerably, ensuring that the mRNA entering the channel is unpaired. Interestingly, two mitochondria-specific proteins, mS26 and mS35, extend along the mRNA channel from its entry region to the opposite mtSSU pole, where the exit site is (Fig 2B).

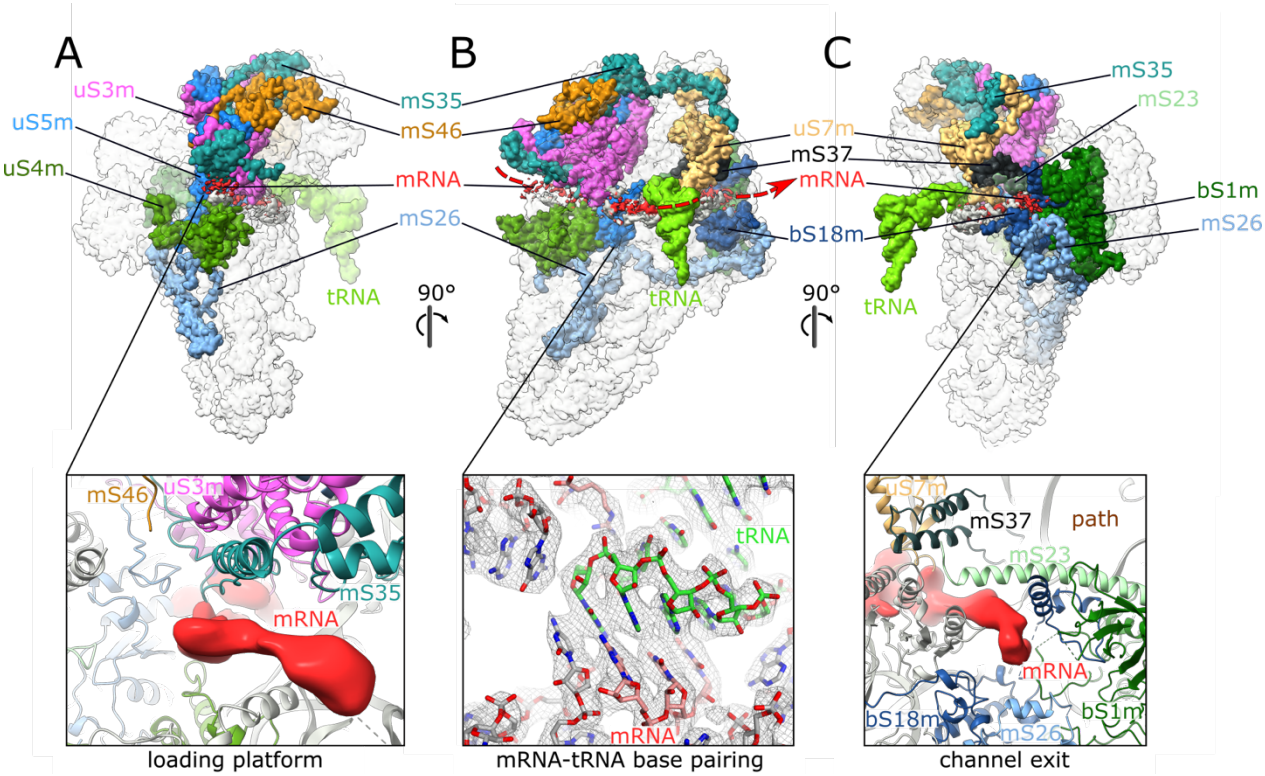

Figure 2. The mRNA channel traced with the density. (A) The density for mRNA (red) reveals a protein platform formed by mS35, mS46 and extensions of uS3m and uS5m. (B) The overall path taken by mRNA is indicated based on the additional density associated with the mtSSU, and codon-anticodon base pairings at the decoding center shown with density. (C) At the exit site, proteins uS7m, bS18m, mS23, mS26, and mS37 are in contact with mRNA, and bS1m is permanently bound. A putative alternative path is indicated.

The channel exit site typically resides at the 3′ end of the rRNA. In the fungal mitoribosome, it has not been significantly altered. The remodeling reported in *S. cerevisiae* does not occur, and therefore represents either a dormant state or species-specific feature. In addition to the conserved proteins, mitochondria-specific mS23, mS26, and mS37 shape the path for mRNA movement (Fig 2C). The C-terminal extension of uS7m narrows the channel, and protein bS18m, mS23, mS26, and mS37 interact with the mRNA density directly. The path toward the exit appears to bifurcate into two subways, and each could in principle accommodate a single stranded mRNA. However, the density for the 5' mRNA clearly only follows the path lateral to mS26 that is also surrounded by a positively charged chemical environment. Protein bS1m, which is considered to have one of the most conserved and ancient protein domains with functional importance of unfolding mRNAs for active translation (Qu *et al*, 2012), is permanently bound to the channel exit (Fig 2C).

The mechanism of tRNA translocation involves a new protein in L1 stalk

During translation, tRNAs are translocated between the three sites. Upon peptide-bond formation, the ribosomal subunits rotate with respect to each other, and the tRNA moves to the intermediate hybrid state. The structure comparison between the complexes with P/P and P/E tRNAs reveals

229 sequential rearrangements in the network of mitoribosome-tRNA interactions and allows us to
230 determine how tRNA is moved.

231 In the P/P state, the anticodon of the tRNA forms base pairing with the mRNA in the conserved P-
232 site of the mtSSU (Fig 3 and Fig EV3). Further stabilization is provided by the conserved C-
233 terminal Arg315 of uS9m, which forms salt bridges with the backbone phosphates in the anticodon
234 loop of the tRNA. The conserved H69 of mtLSU interacts with the D-arm of the tRNA. The
235 conformation of P/P tRNA is overall similar to bacteria. The A-site finger, known as a functional
236 attenuator and important for keeping the correct reading frame (Komoda *et al*, 2006), takes in a
237 straight conformation forming the inter-subunit bridge B1a. The conserved G2453 (G2251) and
238 G2454 (G2252) of the P-loop form base pairs with the CCA terminus of the tRNA and the emerging
239 peptide is bound to the terminal A76, waiting for peptidyl transfer to the next incoming aminoacyl-
240 tRNA at the A-site. Thus, the arrangement of structural elements and tRNA in mitochondria of
241 fungi shows a conserved P-site.

242 After peptide transfer occurs, the ribosomal subunits move relative to each other, which is
243 represented by our P/E hybrid structure. In the rotated conformation, the L1 stalk moves to a closed
244 conformation toward the deacylated tRNA in the P/E hybrid state (Fig 3E). By masked refinement
245 on L1 stalk, we improved the density that allowed building its complete model for the first time in
246 any mitoribosome. We identified an additional protein component, namely mL108 (Fig 1B and Fig
247 EV4), which is an unprecedented occurrence in cytoplasmic counterparts. The core of the protein
248 shows a thioredoxin-like fold, which belongs to a small folding family of mitochondrial proteins
249 mS25, mL43, and the complex I subunit NDUFA2/B8, bearing the possibility of a shared
250 evolutional origin. The protein mL108 interacts with both the L1-stalk rRNA and the protein uL1m
251 (Fig 3D). Furthermore, it forms a new inter-subunit bridge with a long C-terminal helix (Fig 3D).

252 The bases A2381 (G2168) and C2348 (G2112) of the stalk rRNA stack on the elbow of the P/E
253 tRNA (Fig 3E). Unlike in bacteria, uL1m does not interact with the P/E tRNA, instead the domain
254 II of uL1m changes its conformation to form a mitoribsome-specific interaction with H82-ES6 in
255 the CP in the rotated state (Fig 3D). Therefore, the subunit rotation is synchronized with the L1
256 stalk movement during tRNA translocation. The terminal adenosine of the P/E tRNA inserts
257 between the conserved G2873 (G2421) and A2874 (C2422) at the E site (Fig 3E). The anticodon
258 arm of the tRNA remains located in the P-site forming the codon-anticodon base pairing with the
259 mRNA resulting in distorted conformation to swing the acceptor arm into the E-site. The disordered
260 N-terminal extension of mS29 gets structured in the rotated state and interacts to the minor groove
261 of the anticodon stem of the P/E tRNA (Fig EV3), suggesting mitochondria-specific regulation of
262 the translation mechanism. The long C-terminal helix of mL108 reaches down to the mtSSU,
263 applying an additional stabilization of the L1 stalk.

264 Upon back rotation of the mtSSU into the non-rotated E/E state, the L1 stalk moves outwards
265 assisting to pull the P/E tRNA into the E/E state, allowing dissociation into the solvent to complete
266 the translocation cycle (Fig 3 and Fig EV3). The protein uL1m thereby detaches from the CP,
267 releasing the domain II of uL1m. The tip of the C-terminal helix of mL108 translates ~20 Å forming
268 a new bridge with mtSSU by slightly changing its curvature. This structural rearrangement during

mtSSU rotation suggests a coordinated movement of the mtSSU rotation and mL108 to the L1 stalk. The involvement of mitochondria-specific elements in coordination of tRNA movement has been recently reported also in other systems (Aibara *et al*, 2020; Kummer & Ban, 2020; Tobiasson & Amunts, 2020).

Taken together, the data enables to describe the tRNA movement on the mitoribosome and a series of related conformational changes. First, the L1 stalk interacts with mtSSU through mL108 thereby sensing the rotation state. This leads to the inward moving of the rRNA part of the L1 stalk to interact with the tRNA. The domain II of uL1m stabilizes the conformation through the mitochondria-specific interactions with the CP, and mS29 N-terminal loop becomes ordered and stabilizes the tRNA in the P/E state, which is disrupted in the following E/E state.

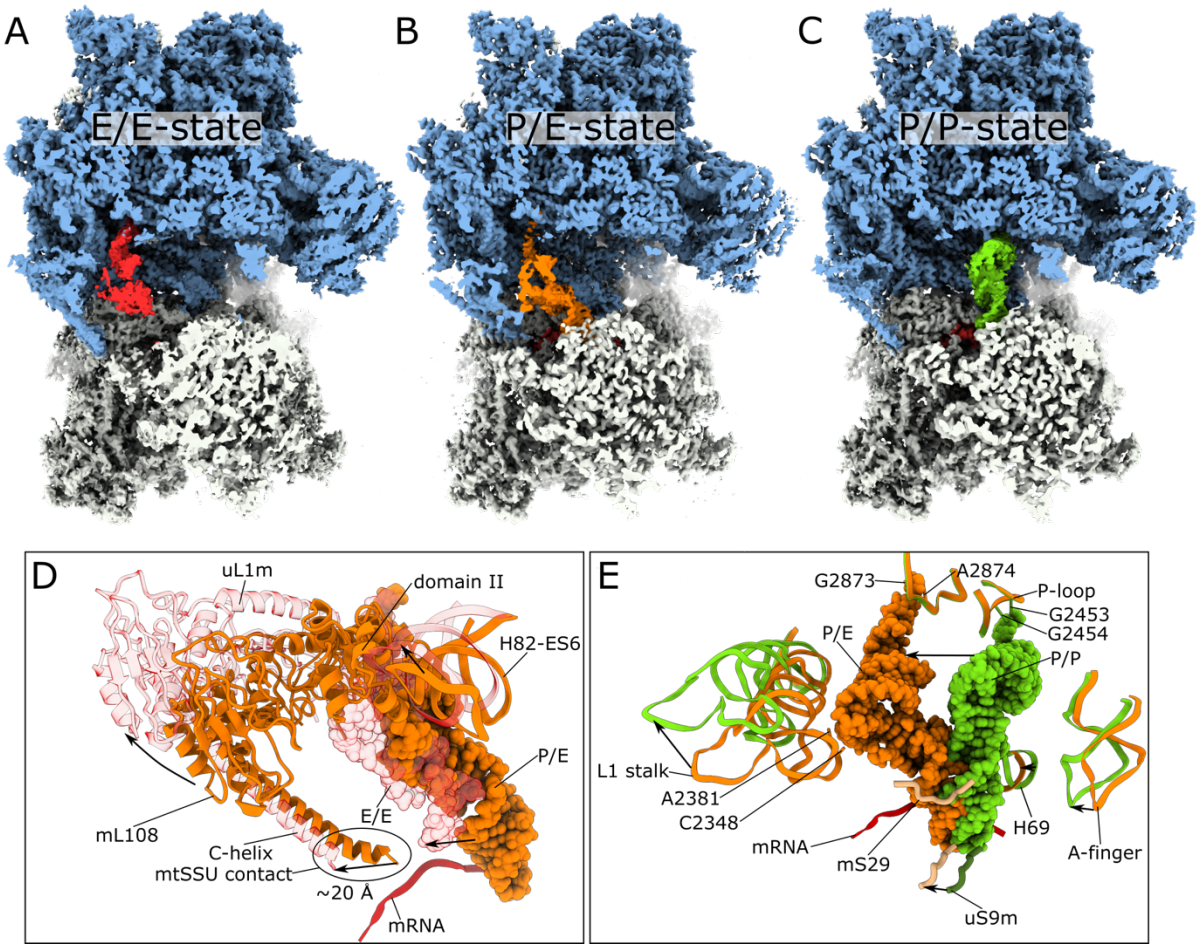

Figure 3. Translocation of tRNA and the L1 stalk. 3D reconstructions of the different states are shown in (A) for the E/E tRNA state (B) for the P/E tRNA state and in (C) for the P/P tRNA state (mtLSU blue; mtSSU gray). (D) Structural rearrangements upon transition between the P/E to E/E states and (E) between the P/P and P/E state are shown. Each two states have been superimposed,

and the affected structural elements are shown according to the text. Movements of the structural elements between the states are indicated by arrows and the contact site to mtSSU is encircled.

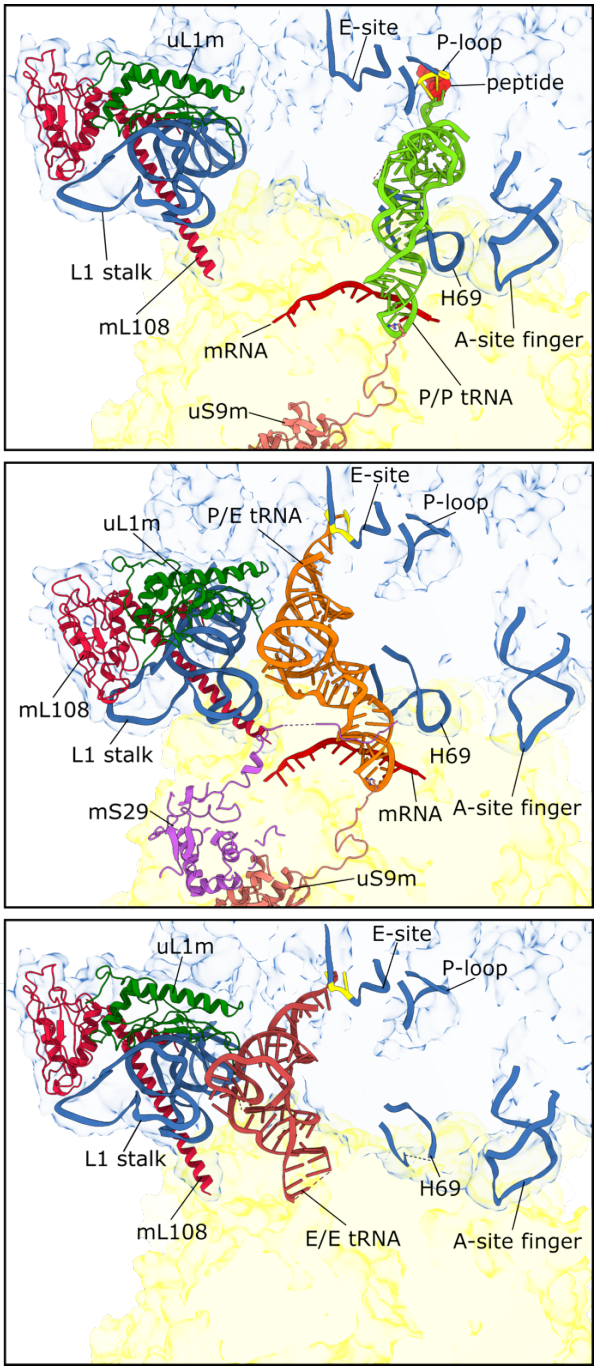

Figure EV3. The L1-stalk and translocation of tRNA. The three states are structurally aligned on mtLSU. Transparent surfaces of mtLSU and mtSSU are colored in blue and yellow respectively. Cartoon representations of important parts are shown and labeled. The P/P-tRNA state with the tRNA colored in green (top panel). The P/E-tRNA state with the tRNA colored in orange (middle panel). The E/E-tRNA state with the tRNA colored in red (bottom panel).

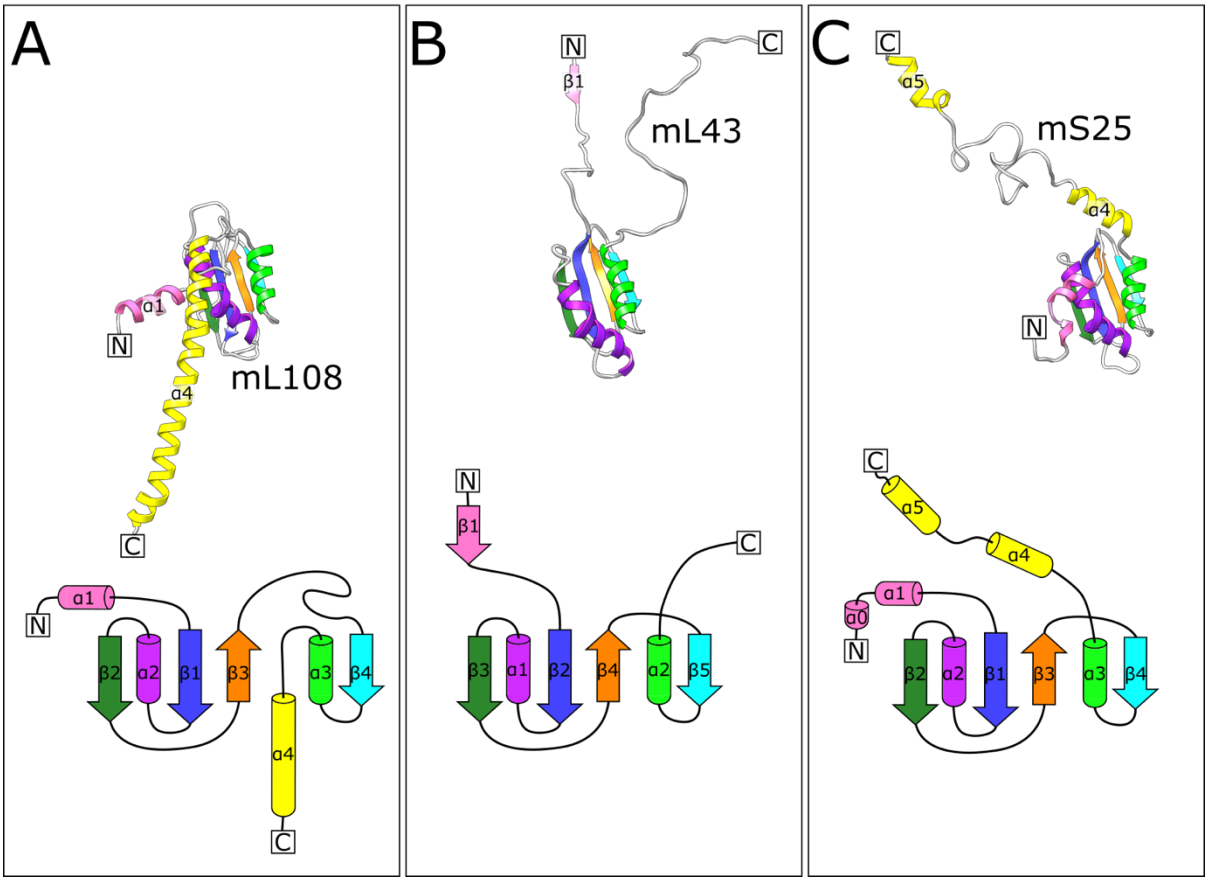

Figure EV4. Topology of mL108, mL43, and mS25. Three dimensional models and topology of the homologous proteins with secondary structure elements colored, featuring their structural similarity. (A) mL108 of *N. crassa*. (B) mL43 of *N. crassa* and (C) mS25 of *Sus scrofa* (PDB ID: 5AJ4).

The nascent polypeptide path to exit the mitoribosome is driven by mitochondria-encoded rRNA reorganisation

As the small mitoribosomal subunit progresses toward the 3' end of the mRNA, the peptidyl transferase center transfers amino acids from tRNAs to the nascent chain, which emerges through the exit tunnel of the large subunit. Therefore, the polypeptide exit tunnel is the defining feature of protein synthesis, and it further facilitates initial folding. Given the fundamental role, the architecture of the tunnel path is among the most conserved features of the ribosome (Dao Duc *et al*, 2019). Against this background, the *S. cerevisiae* mitoribosome structure showed a tunnel path that deviates from the bacterial counterpart, primarily due to rRNA H24 deletion (Amunts *et al.*, 2014). Consequently, the original tunnel was blocked by a specific extension of the mitoribosomal protein uL23m. To what extent the reported structural changes around the mitoribosomal exit tunnel are representative remained an open question. Since the subset of mRNAs subjected to translation in mitochondria from *S. cerevisiae* and *N. crassa* is similar in the way that both

organisms harbor genes that encode for membrane proteins, as well as the soluble mitoribosomal protein uS3m, our analysis reveals the evolutionary drivers for the mitoribosomal exit tunnel adaptation.

For the clarity of the analysis, we partition the tunnel in to two subparts, namely 'upper' that starts with the peptidyl transferase center (PTC) and ends with the uL4m-uL22m constriction site and 'lower' from the constriction site to exit. In our structure, the density for an endogenous polypeptide is detected and the involved structural elements at the upper part of the tunnel are conserved with respect to the geometrical parameters, such as the length (~30 Å) and average radius (~5.3 Å) (Fig 4A). The constriction site between the loops uL4m-uL22m is located 34 Å from the start of the tunnel, and the position correlates well with the *E. coli* ribosome. The density for the nascent polypeptide can be traced from the starting point at the PTC until the beginning of the lower part of the tunnel (Fig 4B).

In the lower part, protein extensions (uL22m, uL23m, uL24m) cluster and occupy the conventional bacteria-like path interior. As a result, although a continuous channel can be traced to the surface of the mitoribosome, the minimal radius of the channel is decreased to 3.3 Å, which represents a considerable narrowing compared to ~6 Å across bacterial ribosomes (Dao Duc *et al.*, 2019) (Fig 4C). We further find side chains that would obstruct the pathway, the majority of which belong to charged amino acids (Fig EV5A). Such occupation would induce an electrostatic Coulomb potential that is inconsistent with hosting hydrophobic polypeptides. Therefore, although the structure maintains the path, the bias toward non-regulated protein growth in the hollow region suggests that the conventional bacteria-like lower part of the tunnel is unlikely to be functional.

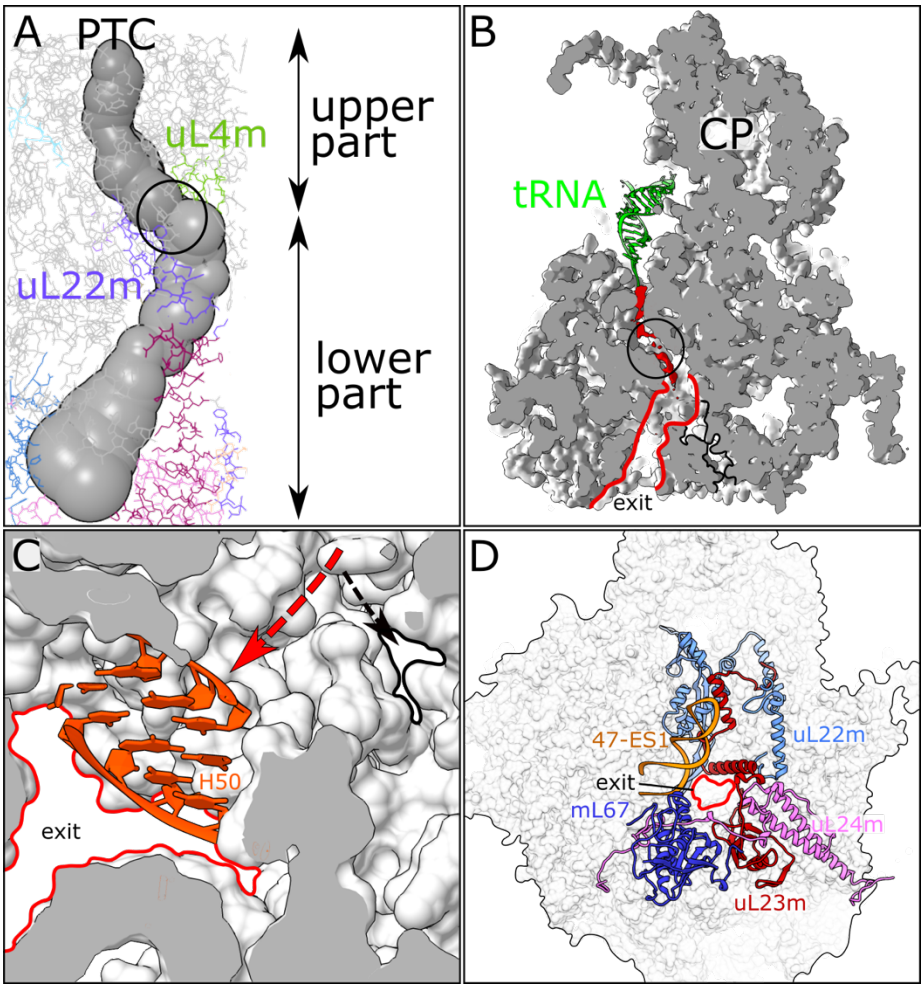

Figure 4. The path of polypeptide of the mitoribosome from *N. crassa*. (A) The calculated tunnel showing the partition of the tunnel in to the upper and lower parts. The constriction site is surrounded by uL22m and uL4m and is labeled by the black circle. (B) Cross-section of the large subunit showing the tunnel with density of the polypeptide reaching from the PTC until the beginning of the lower part of the tunnel. The new tunnel and density of the poly-peptide are colored in red. The constriction site is shown by a black circle and the constricted tunnel is highlighted by a black outline. (C) View of the branching point from inside the tunnel. The red arrow shows the new exit which was formed upon deletion of H50 (orange). The black arrow shows the path of the constricted tunnel. (D) The view of the exit site showing the proteins and rRNA surrounding that region.

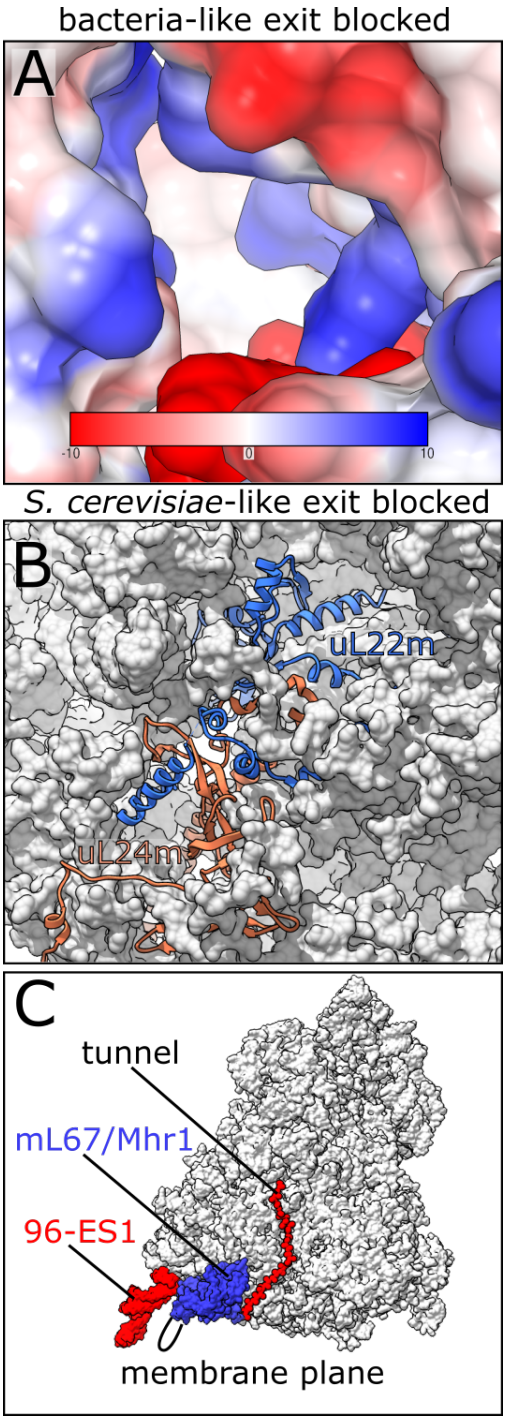

Figure EV5. Analysis of potential exit sites of the tunnel. (A) Surface representation colored by electrostatic Coulomb potential (kcal/mol*e) showing the view of the bacteria-like exit. The path is sterically restricted with positively charged protein environment. (B) Surface representation of the *S. cerevisiae*-like exit. The path is sterically hindered by protein extensions of uL22m and uL24m, shown in cartoon. (C) The polypeptide path in the *N. crassa* mitoribosome. The flexible elements 96-ES1 and mL67/Mhr1 extension around the exit are indicated.

352 To further examine the lower part of the tunnel, we prepared an accurate secondary structure
353 diagram of the mt-rRNA based on the model coordinates (Appendix Fig S6). This was important
354 because the sequence diverges substantially and therefore its alignment is not informative. The
355 comparative analysis of the secondary structure diagrams showed that the 50-nucleotide long
356 reduction of rRNA H24, which was reported to have ignited the remodeling of the tunnel path in
357 the *S. cerevisiae* mitoribosome is also observed in our study (Fig 5). This prompted us to analyze
358 the region of the tunnel path that was shown to involve structural adaptations in *S. cerevisiae.* While
359 the rRNA occupying this region is generally conserved, proteins uL22m and uL24m are extended
360 in their N-termini so that two helical elements prevent accessibility (Fig EV5B). Therefore, the
361 yeast-like tunnel path is obstructed by the mitoribosomal proteins and is unlikely to be functional.

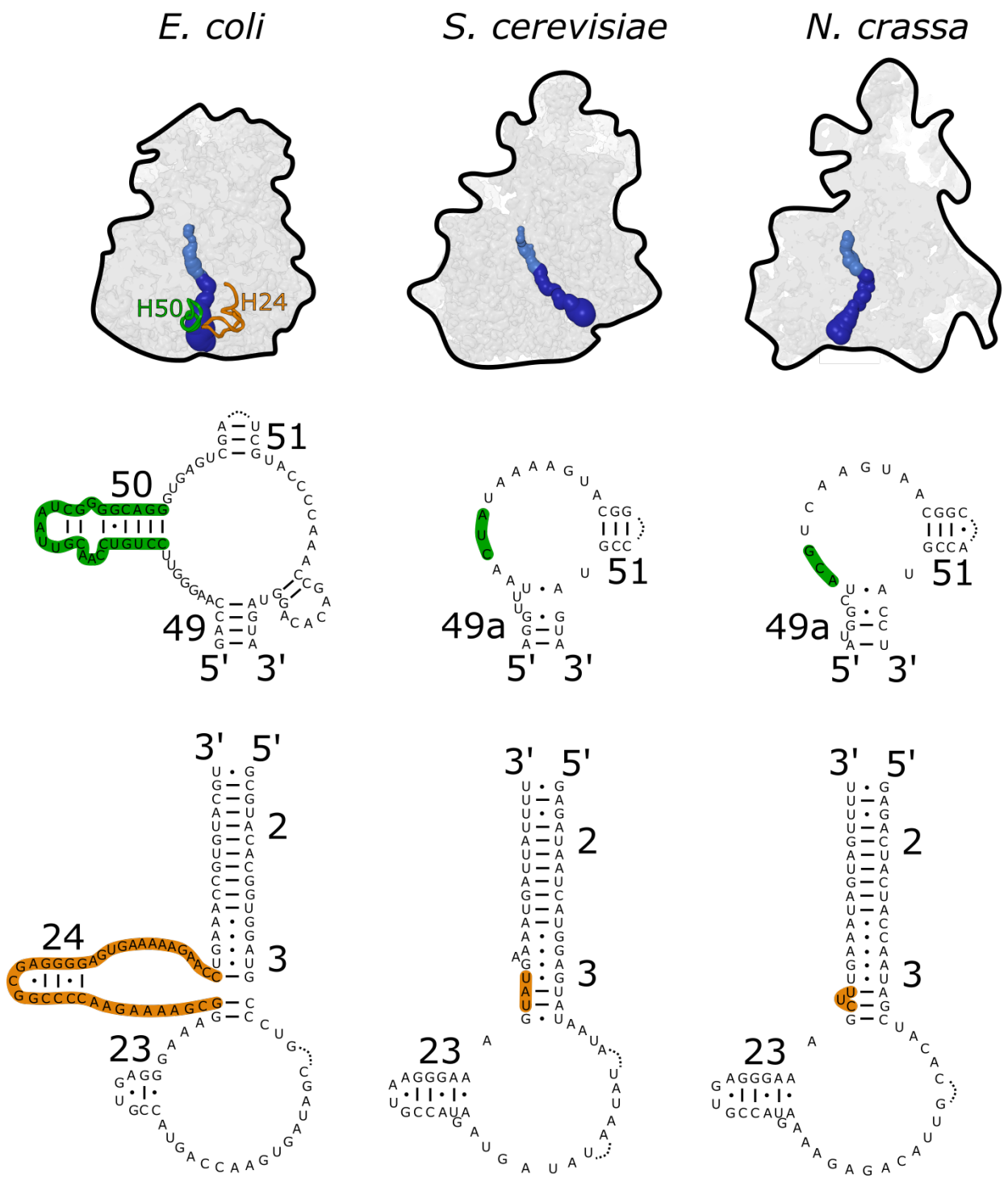

Figure 5. Comparison of the tunnel paths and the rRNA secondary structure elements involved in its formation. The different tunnel paths are shown for the bacterial ribosome (*E. coli*) and the mitoribosomes from *S. cerevisiae* and *N. crassa*. The locations of the rRNA helices H24 (orange) and H50 (green) are indicated. The secondary structure diagram for H24 and H50 regions features their deletion from the sequence of the mitochondrial DNA in *S. cerevisiae* and *N. crassa.*

369 Next, we inspected other remodeling of rRNA in the proximity to the tunnel. We identified a
370 deletion of the 28-nucleotide long rRNA H50 segment ~58 Å from the start of the tunnel (Fig 4C
371 and Fig 5). This remodeling gives rise to a new prominent channel that reaches the mitoribosomal
372 surface ~30 Å away from the original tunnel. The 47-ES1 of the rRNA domain III and the proteins
373 uL22m, uL23m, uL24m, and mL67 shape the boundaries of the tunnel exit leading to the
374 mitoribosomal surface (Fig 4D). Unlike the bacterial-like tunnel, it forms a wide path that would
375 allow a higher degree of conformational sampling for a synthesized protein.

376 The exit site of this newly identified path is further accompanied with specific structural
377 rearrangements. The rRNA element H59 was deleted, and H53 is unstructured and displaced, which
378 is complemented by acquisition of the mitochondria-specific protein mL67/Mhr1. This
379 mitoribosomal protein is also known as mitochondrial recombinase (Ling & Shibata, 2002) that
380 mediates mtDNA replication (Ling & Shibata, 2004), repair (Prasai *et al*, 2017), and was detected
381 in the mitoribosomal assembly survey (Woellhaf *et al*, 2016). It has a flexible extension of 25
382 residues, which is not present in *S. cerevisiae*, adjacent to the exit site and pointing towards the
383 membrane plane (Fig EV5C and Appendix Fig S13). Further, mitochondria-specific rRNA
384 expansion segment 96-ES1 also points towards the membrane and the terminal 39 nucleotides
385 appear to be disordered in our map. Together, the data suggest a potential adaptation of the tunnel
386 exit (Fig EV5C).

387 From the evolutionary perspective, the internal changes that have led to the deviation of the tunnel
388 path are intrinsic to the rRNA fold. As in the case of the *S. cerevisiae* mitoribosome, the path was
389 altered as a result of a deletion in rRNA. Since rRNA is encoded in the mitochondrial genome, it
390 is the loss of genetic material from mitochondria that leads to a considerable effect on the
391 mitoribosomal structure in the exit tunnel. This determines the geometry of the lower tunnel, which
392 is reflected in the protein folding (Kudva *et al*, 2018). Therefore, a further adaptation is required
393 by the means of added protein (mL67/Mhr1) and rRNA (96-ES1) that gain function for the
394 adjustment of the new exit site in respect to the membrane. Consequently, our structure suggests
395 that constructive neutral evolution of mitochondrial DNA (Stoltzfus, 2012) drives the architecture
396 of the mitoribosomal exit tunnel. Furthermore, since both mitoribosomes synthesize a similar
397 subset of proteins by employing different exit tunnels, specific characteristics of the mRNA
398 subjected to translation probably do not provide the main factor in the design of the tunnel. Thus,
399 the structural data provides evidence that the functional adaptation, which results in a more
400 proteinaceous exit allowing conformation sampling and nascent polypeptide accessibility, is driven
401 by the rapidly changing mitochondrial DNA.

402

403 **Visualization of mtLSU-Atp25 assembly intermediate suggests a regulatory mechanism**

404 During 3D classification, we recognized a minor population of the particles corresponding to the
405 isolated mtLSU, and subsequent processing resulted in 3.03 Å resolution reconstruction from
406 24,142 particles (Appendix Fig S5). Fitting the mtLSU model revealed an extra density that appears
407 as a protein element forming a heterodimer with uL14m. In addition, rRNA at the interface (38-
408 ES2, H63, H67-71, H80, 82-ES6, H101, PTC) appears as unfolded (Fig 6). Further, the L1 stalk

409 changes to a conformation that is more flexible and the density for bL9m next to L1 stalk is absent,
410 whereas all the other mtLSU proteins are present (Fig. 6A).

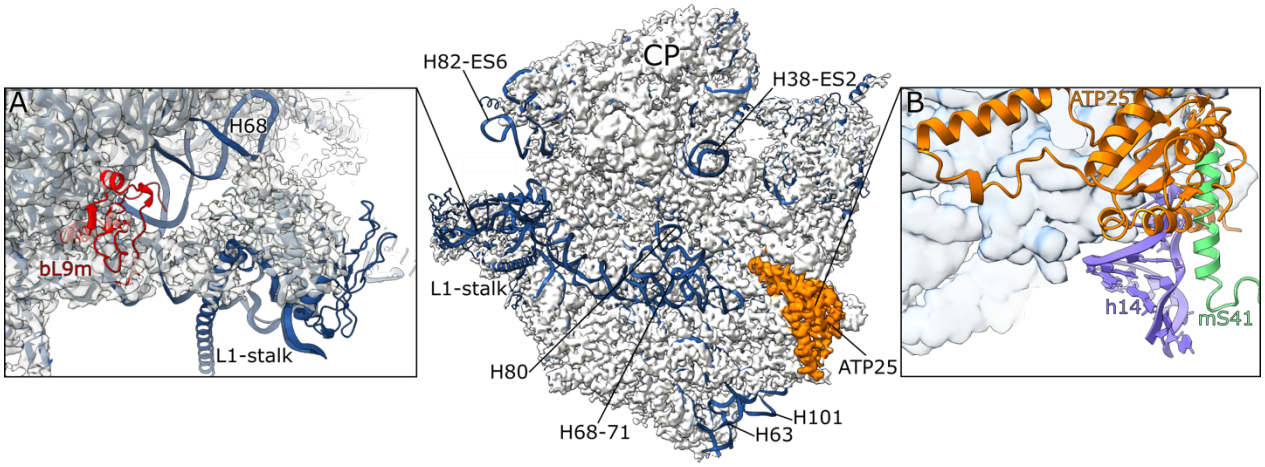

411
412 **Figure 6. Structure and function of the mtLSU-Atp25 assembly complex.** Superposition of the
413 assembly intermediate cryo-EM map (gray) with the mature mtLSU model (blue) reveals unfolded
414 interfacial rRNA. (A) conformational change of the L1 stalk, missing bL9m (red). (B) presence of
415 Atp25 (orange) that would clash with the mtSSU h14 and mS41, preventing subunit association.

416

417 We identified the extra density as Atp25, an ortholog of the bacterial ribosome silencing factor
418 (Rsf), for which there is no high-resolution structural information in complex with a ribosome
419 (Hauser *et al*, 2012; Li *et al*, 2015). Its human mitochondrial counterpart, MALSU1, has been
420 shown to involve late assembly stages (Brown *et al.*, 2017; Rorbach *et al*, 2012). The gene *Atp25*
421 codes for 699 amino acids, including the targeting sequence, an N-terminal part related to
422 Rsf/MALSU1, and a C-terminal part called the M-domain. In *S. cerevisiae*, Atp25 is cleaved
423 between the N- and C-terminal parts during mitochondrial import (Woellhaf *et al.*, 2016) and the
424 M-domain forms a separate functional protein that stabilizes the mRNA of the ATP synthase
425 subunit Atp9 (Zeng *et al*, 2008). The gene fusion is suggested to have evolved in order to prevent
426 off target effects of Atp25 on the cytosolic ribosomes prior to entry to the mitochondria (Woellhaf
427 *et al.*, 2016). We observe only the Rsf/MALSU1-related part of Atp25 on the mitoribosome,
428 confirming the function in the assembly of the mtLSU.

429 Atp25 presents only in the class with the missing bL9m and unfolded interfacial rRNA that affects
430 the L1 stalk. In the mature mitoribosome, bL9m is anchored at the base of the L1 stalk near the E-
431 site, which is stabilized through tertiary interactions with the rRNA. Therefore, the recruitment of
432 bL9m requires specific L1 stalk conformation that is interdependent with rRNA folding, including
433 the PTC.

434 Atp25 bound to uL14m sterically obstructs the binding of the mtSSU by preventing the formation
435 of bridge B8 with its globular domain (Fig 6B). The steric block spans ~25 Å and would clash with
436 h14 of rRNA and the N-terminus of mS26 of the mtSSU. Therefore, the eviction of Atp25 must
437 take place during the final stages of maturation to alleviate the steric hindrance on subunit joining.

438 A similar mechanism was proposed for eIF6 in the cytoplasmic translation apparatus, where protein
439 factor SBDS senses the structural integrity of the functional sites before the displacement (Weis *et*
440 *al*, 2015). Our data imply that since this is a prerequisite step for the folding of interfacial mt-rRNA
441 into a native-like conformation, it is also a requirement for the binding of bL9m. This shows that
442 bL9m attachment is mechanistically regulated during the assembly of the mitoribosome.

443

444 **Conclusions**

445 This study reveals a dedicated mitoribosomal platform for mRNA loading and a newly identified
446 protein mL108 that is associated with the L1 stalk and involved in tRNA translocation. These
447 specific structural features explain the mechanism of translation in mitochondria. The distinct exit
448 tunnel suggests that the evolution of the nascent chain emergence in mitochondria is driven
449 primarily by changes in the rRNA that is encoded in the mitochondrial genome in all species.
450 Finally, the newly described assembly intermediate lacking bL9m proposes a regulatory
451 mechanism.

452

453 **Materials and Methods**

454 **Purification of mitoribosomes**

455 Mitochondria were isolated from *Neurospora crassa* strain K5-15-23-1 (Funes *et al*, 2004) which
456 contains a His-tagged version of Oxa1. The *N. crassa* mycelia were grown in aerobic conditions
457 using 10 L of the Vogel's growth medium (Vogel, 1956), supplemented with L-lysine and L-
458 leucine at 25°C for 16 h. Each growth flask was supplemented with 0.1% chloramphenicol 1 h
459 prior to harvesting. To separate the moisture from the mycelia, the culture was filtered through
460 muslin. The dry mycelia were transferred to a pre-cooled mortar and pestle to lyse the cells. All
461 further operations were performed at 4°C. The cells were lysed using sea-sand (silicon dioxide)
462 and SEMP buffer (250 mM sucrose, 1 mM ethylenediaminetetraacetic acid (EDTA), 10 mM
463 MOPS-KOH pH 7.2, 2 mM phenylmethanesulfonyl fluoride (PMSF), and 0.2% chloramphenicol),
464 by applying a 20 min grinding course. Sand and cell debris were removed using differential
465 centrifugation at low-speed (2000 x g). A subsequent high-speed centrifugation step (17,500 x g)
466 was carried out to sediment crude mitochondria. The mitochondrial pellet was then resuspended in
467 SEM buffer (250 mM sucrose, 1 mM EDTA, and 10 mM MOPS-KOH pH 7.2). To further purify,
468 the crude mitochondria were undergone a sucrose gradient in SEM buffer for 1h at 28,000 rpm
469 with an SW40 Ti rotor (Beckman Coulter). Mitochondrial band was pooled and stored at -80 °C.

470 Mitochondria were lysed in 4 volumes of lysis buffer (25 mM Hepes-KOH pH 7.5, 20 mM KCl,
471 15 mM $Mg(OAc)_2$, 2% *n*-dodecyl-β-D-maltoside (DDM), 0.0075 % cardiolipin, 2 mM
472 dithiothreitol (DTT), 1 tablet of protease inhibitor (cOmplete^{TM}, Roche), and RNase inhibitor
473 (RNaseOUT, Invitrogen)) and incubated for 5 min at 4°C. The membrane was separated by
474 centrifugation of the mitochondrial lysate at 30,000 x g for 20 min followed by a second
475 centrifugation step with the same settings. The supernatant was loaded onto a 1.0 M sucrose
476 cushion in the resuspension buffer (20 mM Hepes-KOH pH 7.5, 15 mM KCL, 15 mM $Mg(OAc)_2$,

477 0.05% DDM, 0.0075% cardiolipin, and 2 mM DTT) with RNase inhibitor and centrifuged at
478 48,000 rpm with a 70 Ti rotor for 4 h. The pellet was then resuspended in the resuspension buffer,
479 loaded on a 15-30% sucrose gradient in the resuspension buffer, and centrifuged at 23,000 rpm
480 with an SW40 Ti for 16 h at 4°C. Fractions containing mitoribosomes were collected and the
481 mitorobosomes were pelleted by centrifugation at 100,000 rpm with a TLA120.2 rotor (Beckman
482 Coulter) for 45 min at 4°C and resuspended in the resuspension buffer.
483
484 **Cryo-EM and image processing**
485 Freshly purified mitorobosome sample (A_{260} = 3.0) was used for grid preparation. 3 µl aliquots of
486 purified mitoribsomes was incubated for 30 s on glow-discharged holey carbon grids (Quantifoil
487 R2/2, 300 mesh, copper) pre-coated with a home-made continuous carbon film with thickness of ~
488 27 Å. The grids were thereafter vitrified in a liquid ethane with a Vitrobot MKIV (FEI/Thermo
489 Fisher) using a blotting time of 3 s at 4°C and 100% humidity. Micrographs were collected with a
490 300 kV Titan Krios (FEI/Thermo Fisher) transmission electron microscope, 70 µm C2 aperture,
491 using a slit width of 20 eV on a GIF-Quantum energy filter (Gatan). A K2 summit detector
492 (GATAN) was used in the counting mode at the calibrated magnification of 130,000 (yielding a
493 pixel size of 1.06 Å). An exposure time of 9 s yielding a total of 35 e/Å^2 was dose fractionated into
494 20 frames. In total 3,172 movies were collected automatically during two consecutive days using
495 EPU (FEI/Thermo Fisher) data collection software. Defocus values ranged between 0.8 and 3.0
496 µm.
497 Collected movie frames were aligned and corrected for both global and non-uniform local beam-
498 induced movements using MotionCor (Li *et al*, 2013) and the contrast transfer function (CTF)
499 parameters were estimated using Gctf (Zhang, 2016), inside the SCIPION program (de la Rosa-
500 Trevin *et al*, 2016). Subsequent data processing steps were performed using RELION-2.1 and 3.0
501 (Kimanius *et al*, 2016). First, 647 particles were manually picked, followed by two-dimensional
502 (2D) classification. Four good 2D class averages were used for reference-based picking for the
503 second round. 265,710 picked particles were subjected to 2D classification and 50 good 2D classes
504 were selected (Appendix Fig S1). Retained 223,605 particles were classified into six classes by
505 three-dimensional (3D) classification, resulted in four good mito-monosome classes (131,806
506 particles), one class with weak mtSSU density (36,053 particles), and one low quality class
507 containing poorly-aligned or broken particles. From the class with weak mtSSU density, isolated
508 mtLSU particles (24,142 particles) are classified out by further 3D classification.
509 Pooled good particles were subjected to 3D auto-refinement. Per-particle CTF refinement (Zivanov
510 *et al*, 2018), followed by Bayesian polishing (Zivanov *et al*, 2019) and the second round of per
511 particle CTF refinement to improve resolution, resulted in reconstructions of mito-monosome and
512 the isolated mtLSU with 2.83 and 3.03 Å resolution, respectively Appendix Fig S1). Resolution is
513 estimated based on the gold standard criterion of Fourier shell correlation (FSC) = 0.143 between
514 the reconstructed two half maps.
515 Due to the relative movement between the mtSSU and mtLSU in monosome, we suffered from low
516 resolution in the mtSSU. We therefore decided to improve the quality of the maps by focused

517 masked refinement for the mtSSU and mtLSU separately. We obtained the masked maps of mtLSU
518 and mtSSU with 2.74 and 2.85 Å resolution, respectively. Further, improvement of local
519 resolutions was achieved by focused refinement using the local masks as described in the
520 Supplementary Material.

521 All the density maps were locally resolution filtered by applying a negative B-factor estimated
522 automatically by RELION-3.0.

523 The observed motion between mtLSU and mtSSU prompted us to separate possible sub-states of
524 the monosome. Firstly, we classified the particles in two major classes (rotated and non-rotated
525 states) by overall 3D classification. To facilitate classifying tRNA states, signal subtraction of
526 ribosome was performed using a cylindrical mask covering the A-, P-, and E-sites for the rotated
527 and non-rotated states separately by RELION 3.0, following by focused 3D classification without
528 alignment. For the rotated state, the same cylindrical mask was applied for the classification, which
529 separated the P/E hybrid tRNA bound mitoribosomes (37,908 particles). For non-rotated state,
530 smaller masks were needed to classify tRNAs. The P/P tRNA bound mitoribosomes were separated
531 applying a mask covering only the P-site, while E/E tRNA bound ones were separated by a mask
532 covering only the E-site. The P/P tRNA and E/E tRNA bound mitoribosomes were 24,611 and
533 23,802 particles, respectively. Among them, only 4,136 particles are overlapping and have both
534 P/P and E/E tRNAs, which are too few for high-resolution reconstruction. Local resolution of the
535 tRNA bound mitoribosomes were also improved by using local masked refinement as described in
536 the Supplementary Material.
537

538 **Model building and refinement**

539 Model building was carried out in Coot (Emsley & Cowtan, 2004). Rigid body docking was carried
540 out in UCSF Chimera (Pettersen *et al*, 2004). The model of the *S. cerevisiae* mitoribosome (PDB
541 ID: 5MRC) was used as a reference. For proteins whose orthologs existed in *S. cerevisiae* structure,
542 the homology models of *N. crassa* were generated by SWISS Model (Waterhouse *et al*, 2018),
543 placed into the density, manually revised and built unmodeled and unique regions, and real space
544 fit in *Coot*. Previously unknown or unmodeled proteins were modeled *de novo* in *Coot*. For the
545 correct assignment of the proteins, sequence stretches of reasonable quality were directly identified
546 from the map and then applied to BLAST (Altschul *et al*, 1990) and/or compared to the protein
547 sequences gained from mass spectrometry (Appendix Table S4). The ribosomal protein mL108
548 was named according to the standard nomenclature widely accepted in the ribosome community
549 (Ban *et al*, 2014). The number was chosen in a chronological order of discover also considering
550 unpublished data. The entire rRNAs, tRNAs, and mRNAs were modeled *de novo* in *Coot*. Since
551 bound tRNAs and mRNAs are mixture of any mitochondrial ones, each residue was assigned as
552 either A, U, G, or C, based on the density and conservation. Ligands and metal ions were placed
553 into the density.

554 For model refinement of the consensus mtLSU and mtSSU and the monosomes in the three tRNA
555 states, the local masked refined maps with B-factor sharpening and local-resolution filtering were
556 merged using the program phenix_combine_focused_maps in the Phenix software suite

(Liebschner *et al*, 2019), thereby generating a map for model refinement. For the isolated mtLSU, the overall refined map with B-factor sharpening and local-resolution filtering was used for model refinement. Refinement of all models was performed using Phenix.rel_space_refine (Afonine *et al*, 2018). The final structure was validated using the MolProbity (Williams *et al*, 2018) implementation of the Phenix suite.

Figure preparation

All structural figures were generated with PyMOL (DeLano, 2002), UCSF Chimera (Pettersen *et al.*, 2004), and ChimeraX (Goddard *et al*, 2018). The secondary structure diagrams of the 16S and 23S rRNA were generated using XRNA (http://rna.ucsc.edu/rnacenter/xrna/xrna.html).The shape of the polypeptide tunnels were calculated with the software Mole(Pravda *et al*, 2018).

Acknowledgements We thank Frank Nargang for providing the *N. crassa* strain, and Marta Carroni and Julian Conrad for supporting cryo-EM data collection. This work was supported by the Swedish Foundation for Strategic Research (FFL15:0325), Ragnar Söderberg Foundation (M44/16), Swedish Research Council (NT_2015-04107), Cancerfonden (2017/1041), European Research Council (ERC-2018-StG-805230), Knut and Alice Wallenberg Foundation (2018.0080), EMBO Young Investigator Program. Y.I. is supported by H2020-MSCA-IF-2017 (799399-Itohribo). The data was collected at the SciLifeLab cryo-EM facility funded by the Knut and Alice Wallenberg, Family Erling Persson, and Kempe foundations. Mass spectrometry analysis was performed by the clinical proteomics mass spectrometry facility of the Karolinska University Hospital and SciLifeLab proteogenomics core facility. We thank John Walker and Alan Brown for constructive comments, and Katrina Albert for proofreading the manuscript.

Author contributions A.A. designed the project. N.M prepared the sample and collected cryo-EM data. Y.I., A.N. and N.M. processed the data and built the model. Y.I., A.N. and A.A. wrote the manuscript with help from N.M. and J.M.H.

Conflict of interests The authors declare no conflict of interests.

Data availability

Cryo-EM maps have been deposited at the EMDB with the following accession codes: EMD-10958, EMD-10961, EMD-10962, EMD-10963, EMD-10965, EMD-10966, EMD-10967, EMD-10968, EMD-10969, EMD-10970, EMD-10971, EMD-10972 EMD-10973, EMD-10974, EMD-10975, EMD-10976, EMD-10977, EMD-10978, EMD-10979, EMD-10980, EMD-10981, EMD-10982, EMD-10983, EMD-10984, EMD-10985, EMD-10986, EMD-10988, EMD-10989, EMD-10990, EMD-10991 and EMD-10992. The atomic coordinates have been deposited at the PDB with the following accession codes: 6YWS, 6YW5, 6YWX, 6YWY, 6YWE and 6YWV.

References

Afonine PV, Poon BK, Read RJ, Sobolev OV, Terwilliger TC, Urzhumtsev A, Adams PD (2018) Real-space refinement in PHENIX for cryo-EM and crystallography. *Acta Crystallogr D Struct Biol* 74: 531-544

Aibara S, Andrell J, Singh V, Amunts A (2018) Rapid Isolation of the Mitoribosome from HEK Cells. *J Vis Exp*

Aibara S, Modelska A, Singh V, Amunts A (2020) Structural basis of mitochondrial translation. *Elife*: in press

Altschul SF, Gish W, Miller W, Myers EW, Lipman DJ (1990) Basic local alignment search tool. *J Mol Biol* 215: 403-410

Amunts A, Brown A, Bai XC, Llacer JL, Hussain T, Emsley P, Long F, Murshudov G, Scheres SHW, Ramakrishnan V (2014) Structure of the yeast mitochondrial large ribosomal subunit. *Science* 343: 1485-1489

Amunts A, Brown A, Toots J, Scheres SHW, Ramakrishnan V (2015) Ribosome. The structure of the human mitochondrial ribosome. *Science* 348: 95-98

Ban N, Beckmann R, Cate JH, Dinman JD, Dragon F, Ellis SR, Lafontaine DL, Lindahl L, Liljas A, Lipton JM *et al* (2014) A new system for naming ribosomal proteins. *Curr Opin Struct Biol* 24: 165-169

Bason JV, Montgomery MG, Leslie AG, Walker JE (2014) Pathway of binding of the intrinsically disordered mitochondrial inhibitor protein to F1-ATPase. *Proc Natl Acad Sci U S A* 111: 11305-11310

Brown A, Amunts A, Bai XC, Sugimoto Y, Edwards PC, Murshudov G, Scheres SHW, Ramakrishnan V (2014) Structure of the large ribosomal subunit from human mitochondria. *Science* 346: 718-722

Brown A, Rathore S, Kimanius D, Aibara S, Bai XC, Rorbach J, Amunts A, Ramakrishnan V (2017) Structures of the human mitochondrial ribosome in native states of assembly. *Nat Struct Mol Biol* 24: 866-869

Cabezon E, Montgomery MG, Leslie AG, Walker JE (2003) The structure of bovine F1-ATPase in complex with its regulatory protein IF1. *Nat Struct Biol* 10: 744-750

Cabezon E, Runswick MJ, Leslie AG, Walker JE (2001) The structure of bovine IF(1), the regulatory subunit of mitochondrial F-ATPase. *EMBO J* 20: 6990-6996

Dao Duc K, Batra SS, Bhattacharya N, Cate JHD, Song YS (2019) Differences in the path to exit the ribosome across the three domains of life. *Nucleic Acids Res* 47: 4198-4210

de la Rosa-Trevin JM, Quintana A, Del Cano L, Zaldivar A, Foche I, Gutierrez J, Gomez-Blanco J, Burguet-Castell J, Cuenca-Alba J, Abrishami V *et al* (2016) Scipion: A software framework toward integration, reproducibility and validation in 3D electron microscopy. *J Struct Biol* 195: 93-99

DeLano WL (2002) Pymol: An open-source molecular graphics tool. . *CCP4 Newsletter On Protein Crystallography* 40: 82-92

Desai N, Brown A, Amunts A, Ramakrishnan V (2017) The structure of the yeast mitochondrial ribosome. *Science* 355: 528-531

Emsley P, Cowtan K (2004) Coot: model-building tools for molecular graphics. *Acta Crystallogr D Biol Crystallogr* 60: 2126-2132

Funes S, Nargang FE, Neupert W, Herrmann JM (2004) The Oxa2 protein of Neurospora crassa plays a critical role in the biogenesis of cytochrome oxidase and defines a ubiquitous subbranch of the Oxa1/YidC/Alb3 protein family. *Mol Biol Cell* 15: 1853-1861

Goddard TD, Huang CC, Meng EC, Pettersen EF, Couch GS, Morris JH, Ferrin TE (2018) UCSF ChimeraX: Meeting modern challenges in visualization and analysis. *Protein Sci* 27: 14-25

Greber BJ, Bieri P, Leibundgut M, Leitner A, Aebersold R, Boehringer D, Ban N (2015) Ribosome. The complete structure of the 55S mammalian mitochondrial ribosome. *Science* 348: 303-308

Greber BJ, Boehringer D, Leitner A, Bieri P, Voigts-Hoffmann F, Erzberger JP, Leibundgut M, Aebersold R, Ban N (2014) Architecture of the large subunit of the mammalian mitochondrial ribosome. *Nature* 505: 515-519

Hauser R, Pech M, Kijek J, Yamamoto H, Titz B, Naeve F, Tovchigrechko A, Yamamoto K, Szaflarski W, Takeuchi N *et al* (2012) RsfA (YbeB) proteins are conserved ribosomal silencing factors. *PLoS Genet* 8: e1002815

Kim HJ, Maiti P, Barrientos A (2017) Mitochondrial ribosomes in cancer. *Semin Cancer Biol* 47: 67-81

Kimanius D, Forsberg BO, Scheres SH, Lindahl E (2016) Accelerated cryo-EM structure determination with parallelisation using GPUs in RELION-2. *Elife* 5

Komoda T, Sato NS, Phelps SS, Namba N, Joseph S, Suzuki T (2006) The A-site finger in 23 S rRNA acts as a functional attenuator for translocation. *J Biol Chem* 281: 32303-32309

Kudva R, Tian P, Pardo-Avila F, Carroni M, Best RB, Bernstein HD, von Heijne G (2018) The shape of the bacterial ribosome exit tunnel affects cotranslational protein folding. *Elife* 7

Kummer E, Ban N (2020) Structural insights into mammalian mitochondrial translation elongation catalyzed by mtEFG1. *EMBO J*: e104820

Kuntzel H (1969) Mitochondrial and cytoplasmic ribosomes from Neurospora crassa: characterization of their subunits. *J Mol Biol* 40: 315-320

Kuntzel H, Noll H (1967) Mitochondrial and cytoplasmic polysomes from Neurospora crassa. *Nature* 215: 1340-1345

Li X, Mooney P, Zheng S, Booth CR, Braunfeld MB, Gubbens S, Agard DA, Cheng Y (2013) Electron counting and beam-induced motion correction enable near-atomic-resolution single-particle cryo-EM. *Nat Methods* 10: 584-590

Li X, Sun Q, Jiang C, Yang K, Hung LW, Zhang J, Sacchettini JC (2015) Structure of Ribosomal Silencing Factor Bound to Mycobacterium tuberculosis Ribosome. *Structure* 23: 2387

Liebschner D, Afonine PV, Baker ML, Bunkoczi G, Chen VB, Croll TI, Hintze B, Hung LW, Jain S, McCoy AJ *et al* (2019) Macromolecular structure determination using X-rays, neutrons and electrons: recent developments in Phenix. *Acta Crystallogr D Struct Biol* 75: 861-877

Ling F, Shibata T (2002) Recombination-dependent mtDNA partitioning: in vivo role of Mhr1p to promote pairing of homologous DNA. *EMBO J* 21: 4730-4740

Ling F, Shibata T (2004) Mhr1p-dependent concatemeric mitochondrial DNA formation for generating yeast mitochondrial homoplasmic cells. *Mol Biol Cell* 15: 310-322

Nargang FE, Preuss M, Neupert W, Herrmann JM (2002) The Oxa1 protein forms a homooligomeric complex and is an essential part of the mitochondrial export translocase in Neurospora crassa. *J Biol Chem* 277: 12846-12853

Neupert W, Sebald W, Schwab AJ, Massinger P, Bucher T (1969) Incorporation in vivo of 14C-labelled amino acids into the proteins of mitochondrial ribosomes from Neurospora crassa sensitive to cycloheximide and insensitive to Chloramphenicol. *Eur J Biochem* 10: 589-591

Petrov AS, Wood EC, Bernier CR, Norris AM, Brown A, Amunts A (2019) Structural Patching Fosters Divergence of Mitochondrial Ribosomes. *Mol Biol Evol* 36: 207-219

Pettersen EF, Goddard TD, Huang CC, Couch GS, Greenblatt DM, Meng EC, Ferrin TE (2004) UCSF Chimera--a visualization system for exploratory research and analysis. *J Comput Chem* 25: 1605-1612

Prasai K, Robinson LC, Scott RS, Tatchell K, Harrison L (2017) Evidence for double-strand break mediated mitochondrial DNA replication in Saccharomyces cerevisiae. *Nucleic Acids Res* 45: 7760-7773

Pravda L, Sehnal D, Tousek D, Navratilova V, Bazgier V, Berka K, Svobodova Varekova R, Koca J, Otyepka M (2018) MOLEonline: a web-based tool for analyzing channels, tunnels and pores (2018 update). *Nucleic Acids Res* 46: W368-W373

Qu X, Lancaster L, Noller HF, Bustamante C, Tinoco I, Jr. (2012) Ribosomal protein S1 unwinds double-stranded RNA in multiple steps. *Proc Natl Acad Sci U S A* 109: 14458-14463

Robinson GC, Bason JV, Montgomery MG, Fearnley IM, Mueller DM, Leslie AG, Walker JE (2013) The structure of F(1)-ATPase from Saccharomyces cerevisiae inhibited by its regulatory protein IF(1). *Open Biol* 3: 120164

Rorbach J, Gammage PA, Minczuk M (2012) C7orf30 is necessary for biogenesis of the large subunit of the mitochondrial ribosome. *Nucleic Acids Res* 40: 4097-4109

Stoltzfus A (2012) Constructive neutral evolution: exploring evolutionary theory's curious disconnect. *Biol Direct* 7: 35

Tobiasson V, Amunts A (2020) Ciliate mitoribosome illuminates evolutionary steps of mitochondrial translation. *Elife* 9

van der Sluis EO, Bauerschmitt H, Becker T, Mielke T, Frauenfeld J, Berninghausen O, Neupert W, Herrmann JM, Beckmann R (2015) Parallel Structural Evolution of Mitochondrial Ribosomes and OXPHOS Complexes. *Genome Biol Evol* 7: 1235-1251

Vogel HJ (1956) A convenient growth medium for Neurospora crassa. *Microbial Genet Bull* 13: 42-43

Waterhouse A, Bertoni M, Bienert S, Studer G, Tauriello G, Gumienny R, Heer FT, de Beer TAP, Rempfer C, Bordoli L *et al* (2018) SWISS-MODEL: homology modelling of protein structures and complexes. *Nucleic Acids Res* 46: W296-W303

Weis F, Giudice E, Churcher M, Jin L, Hilcenko C, Wong CC, Traynor D, Kay RR, Warren AJ (2015) Mechanism of eIF6 release from the nascent 60S ribosomal subunit. *Nat Struct Mol Biol* 22: 914-919

Williams CJ, Headd JJ, Moriarty NW, Prisant MG, Videau LL, Deis LN, Verma V, Keedy DA, Hintze BJ, Chen VB *et al* (2018) MolProbity: More and better reference data for improved all-atom structure validation. *Protein Sci* 27: 293-315

Woellhaf MW, Sommer F, Schroda M, Herrmann JM (2016) Proteomic profiling of the mitochondrial ribosome identifies Atp25 as a composite mitochondrial precursor protein. *Mol Biol Cell* 27: 3031-3039

Zeng X, Barros MH, Shulman T, Tzagoloff A (2008) ATP25, a new nuclear gene of Saccharomyces cerevisiae required for expression and assembly of the Atp9p subunit of mitochondrial ATPase. *Mol Biol Cell* 19: 1366-1377

Zhang K (2016) Gctf: Real-time CTF determination and correction. *J Struct Biol* 193: 1-12

Zivanov J, Nakane T, Forsberg BO, Kimanius D, Hagen WJ, Lindahl E, Scheres SH (2018) New tools for automated high-resolution cryo-EM structure determination in RELION-3. *Elife* 7

Zivanov J, Nakane T, Scheres SHW (2019) A Bayesian approach to beam-induced motion correction in cryo-EM single-particle analysis. *IUCrJ* 6: 5-17

Appendix

Analysis of translating mitoribosome reveals functional characteristics of protein synthesis in mitochondria of fungi

Yuzuru Itoh[1,2†], Andreas Naschberger[1†], Narges Mortezaei[1†], Johannes Herrmann[3] and Alexey Amunts[1,2*]

[1]Science for Life Laboratory, Department of Biochemistry and Biophysics, Stockholm University, 17165 Solna, Sweden

[2]Department of Medical Biochemistry and Biophysics, Karolinska Institutet, 17165 Solna, Sweden

[3]Cell Biology, University of Kaiserslautern, Erwin-Schrödinger-Straße 13, 67663 Kaiserslautern, Germany

† These authors contributed equally to this work.

*Correspondence and request for material should be addressed to amunts@scilifelab.se

This file includes:

Appendix Figures S1 to S13

Appendix Tables S1 to S4

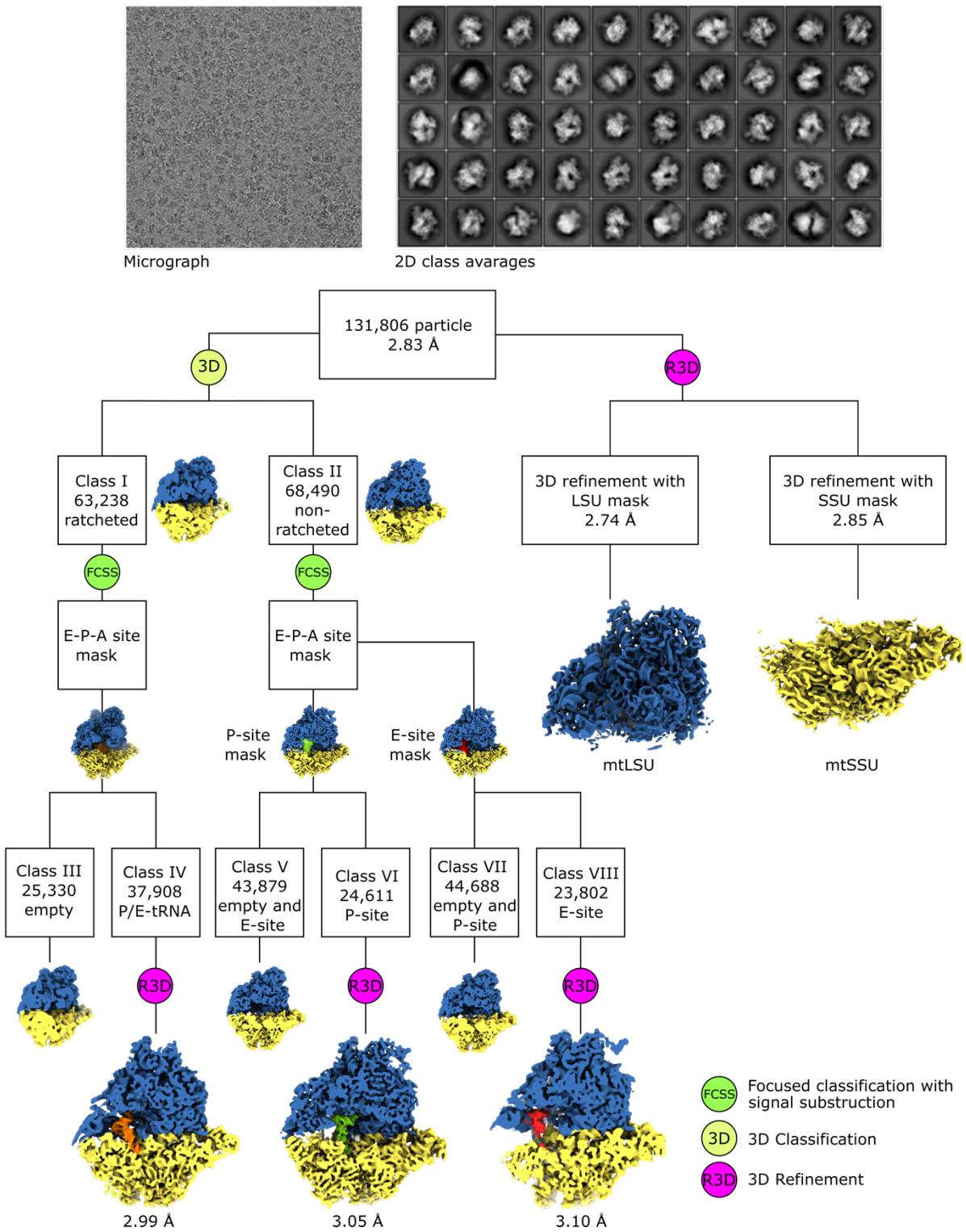

Appendix Figure S1. Cryo-EM data collection and processing scheme. Representative micrograph and 2D class averages. Data refinement protocol and classification scheme for mtLSU, mtSSU and monosome in three tRNA bound states.

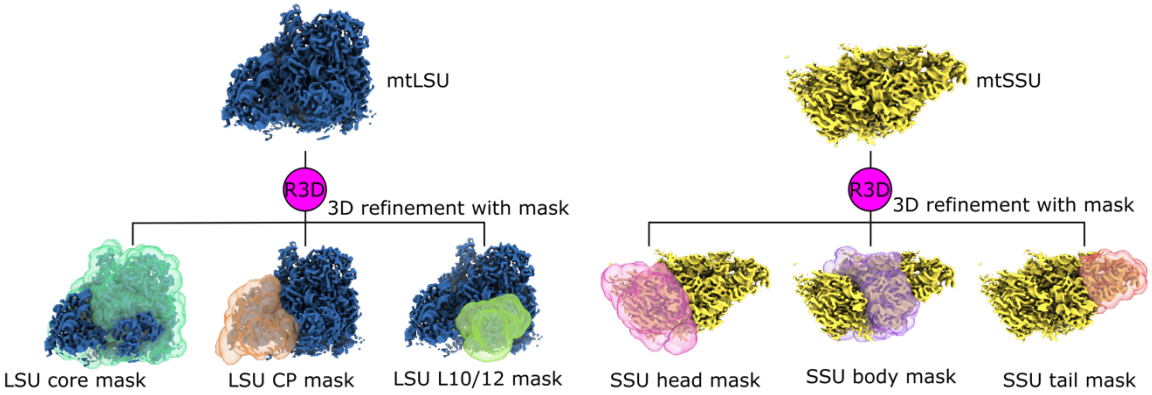

725

726 **Appendix Figure S2. Masked refinement of mitoribosomal subunits.** Masks for mtLSU core,
727 CP, L7/12 stalk; mtSSU head, body, tail were used to improve the density locally.

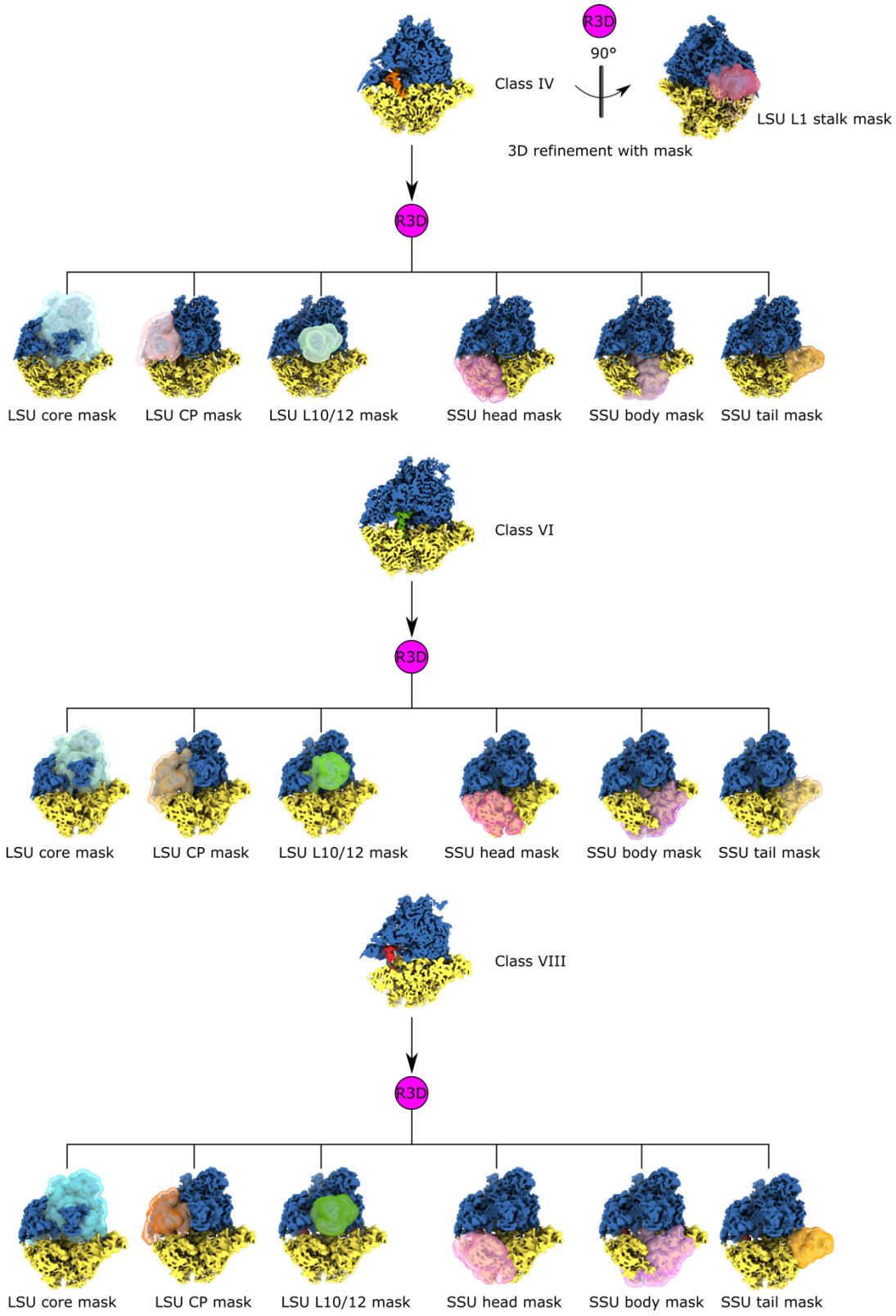

Appendix Figure S3. Masking refinement of the mitoribosomes in tRNA bound states.

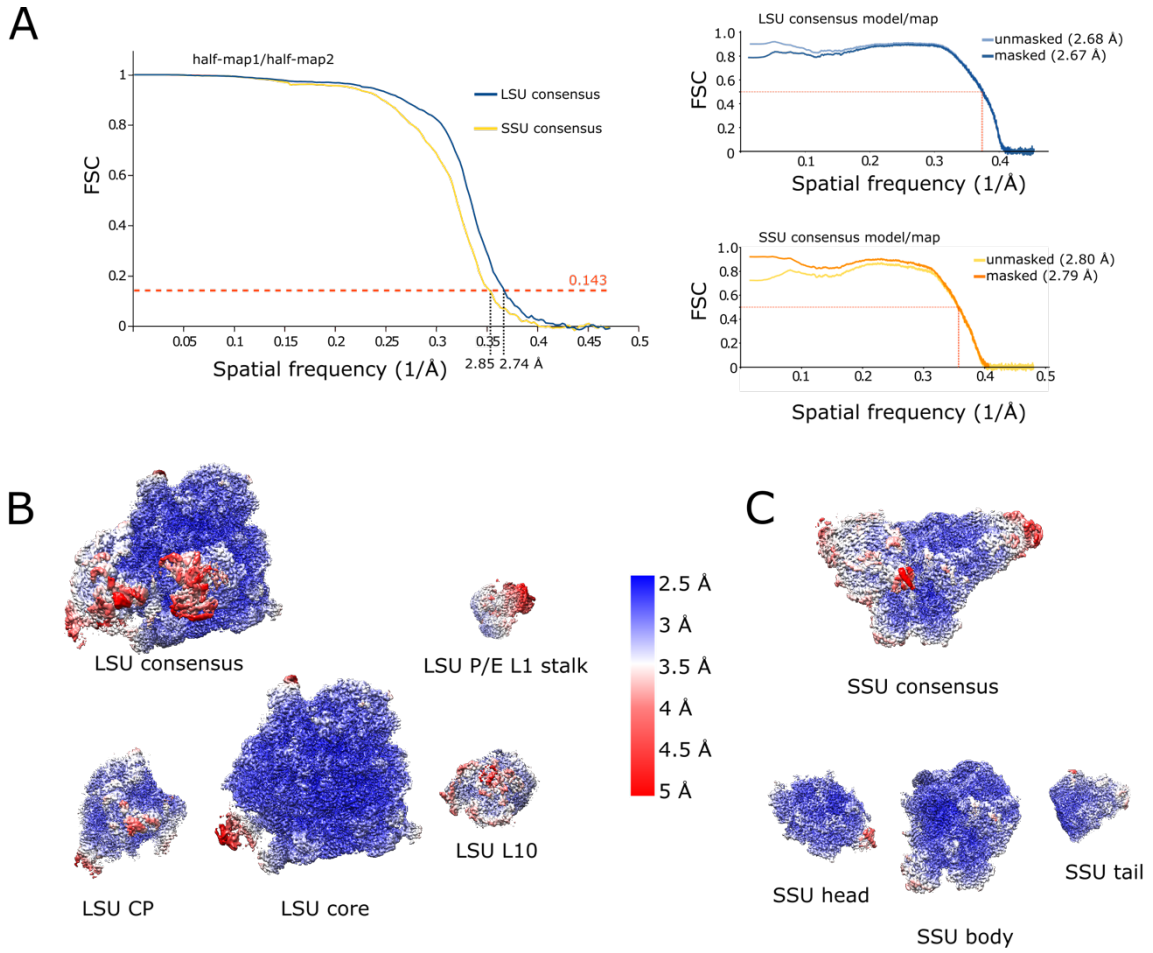

Appendix Figure S4. Overall and local resolution estimations of mitoribosomal subunits. A, Fourier Shell Correlation (FSC) curves of half-maps and map-to-model are shown. Cut-off values of 0.143 (gold-standard) and 0.5 (model-to-map) are indicated and the corresponding resolution estimates are shown **B,** mtLSU cryo-EM maps viewed according to local resolution. C**,** mtSSU cryo-EM maps viewed according to local resolution.

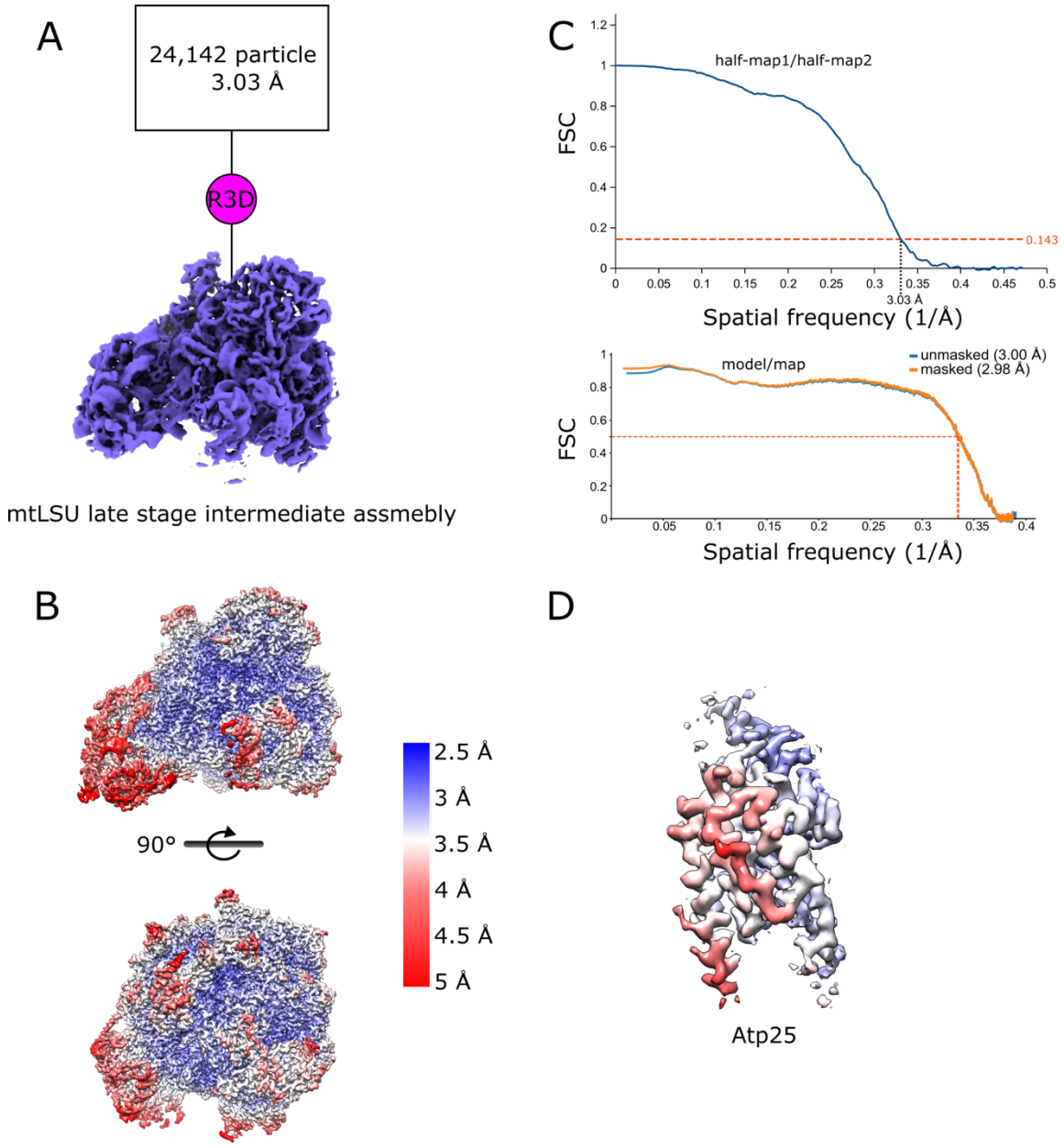

Appendix Figure S5. Data processing and overall and local resolution estimations of mtLSU-Atp25 assembly intermediate. (A) Processing scheme. (B) Fourier Shell Correlation (FSC) curves for half-maps and map-to-model are shown. Cut-off values are indicated and resolution estimates are shown. (C) mtLSU-Atp25 assembly intermediate cryo-EM maps colored according to local resolution. (D) Zoomed in map for Atp25 colored by local resolution.

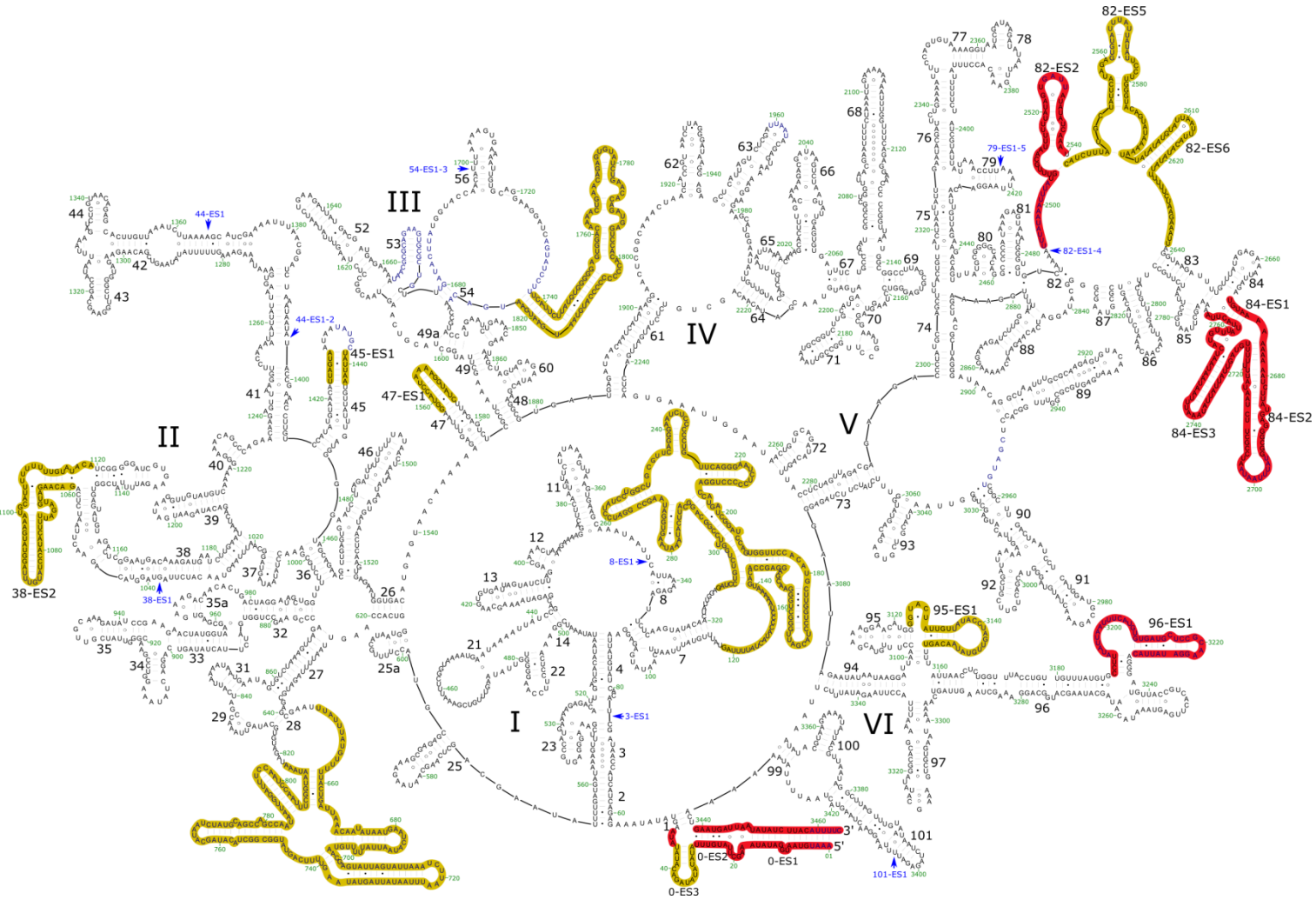

743

744 **Appendix Figure S6. Structure-based secondary structure diagram of the mtLSU rRNA.** Expansion segments shared between *N.*
745 *crassa* and *S. cerevisiae* are highlighted with red, specific expansion segments are highlighted with yellow. Those present in *S. cerevisiae*
746 only are indicated by light blue arrows. rRNA somains are labeled with roman numerals.

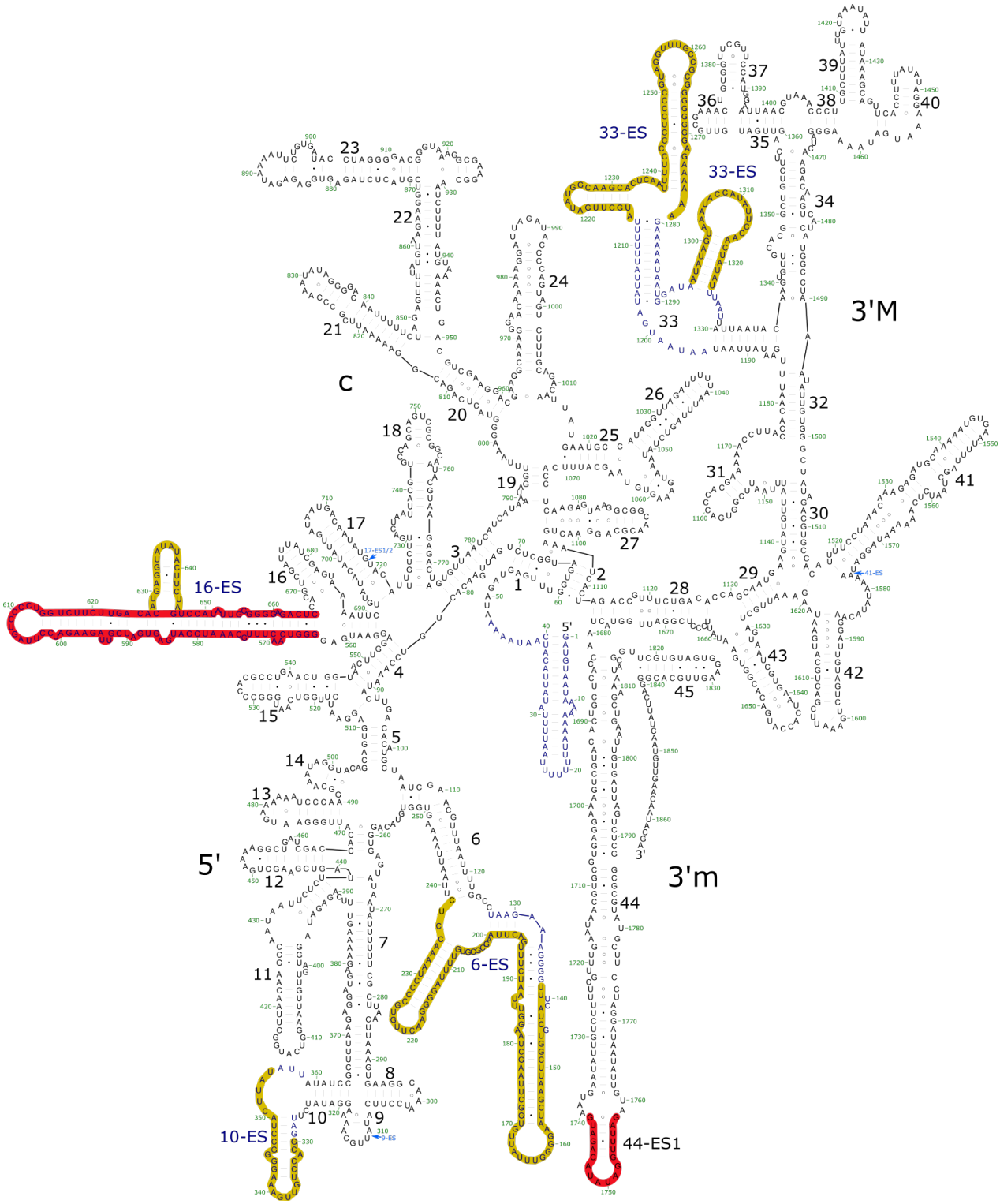

Appendix Figure S7. Structure-based secondary structure diagram of the mtLSU rRNA. Expansion segments shared between *N. crassa* and *S. cerevisiae* are highlighted with red, specific expansion segments are highlighted with yellow. Those present in *S. cerevisiae* only are indicated by light blue arrows. rRNA domains are labeled with roman numerals.

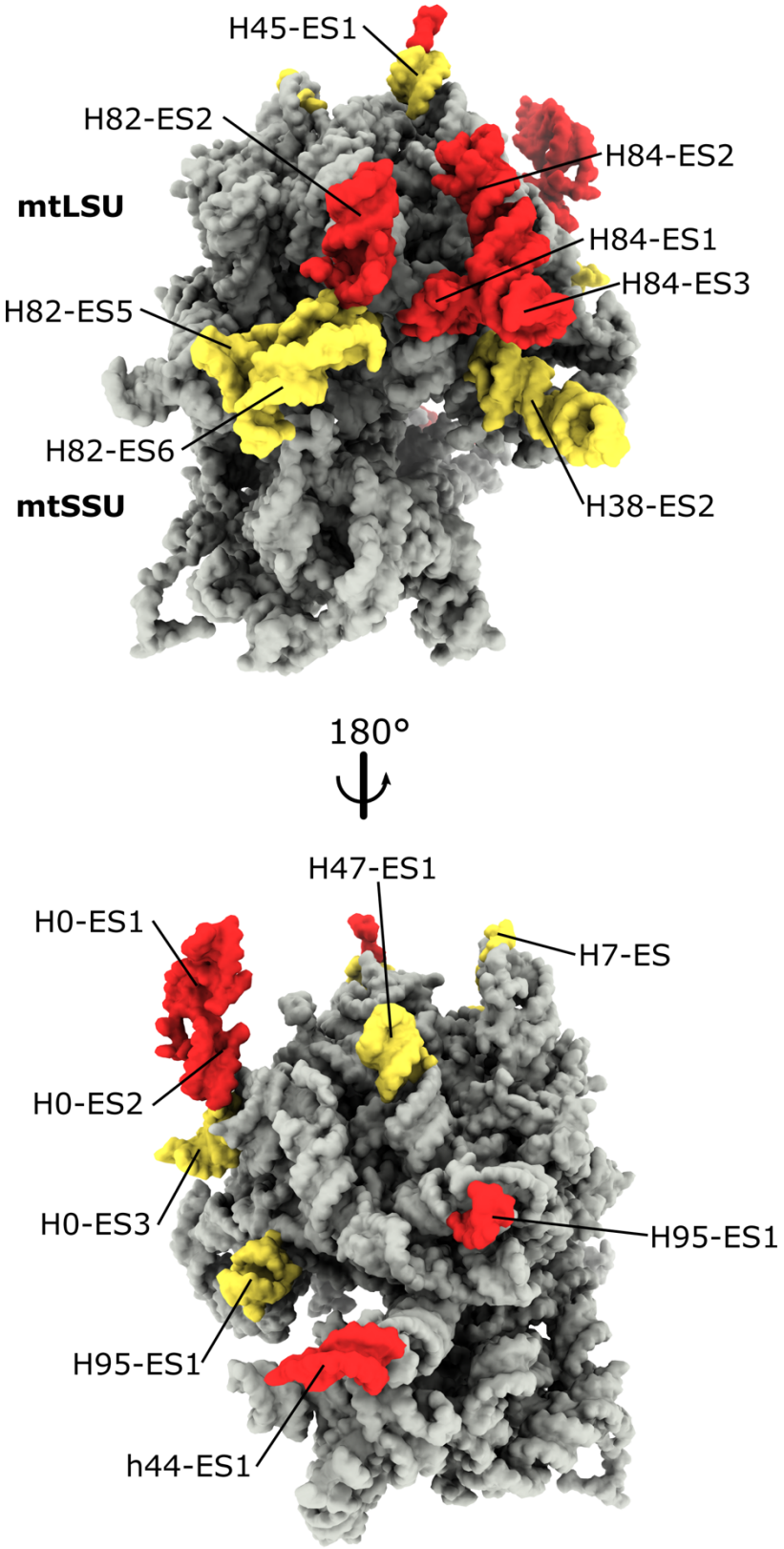

Appendix Figure S8. 3D view of the rRNA of mtLSU and mtSSU. The conserved rRNA is in gray. ESs shared with *S. cerevisiae* are in red, and specific ESs in yellow.

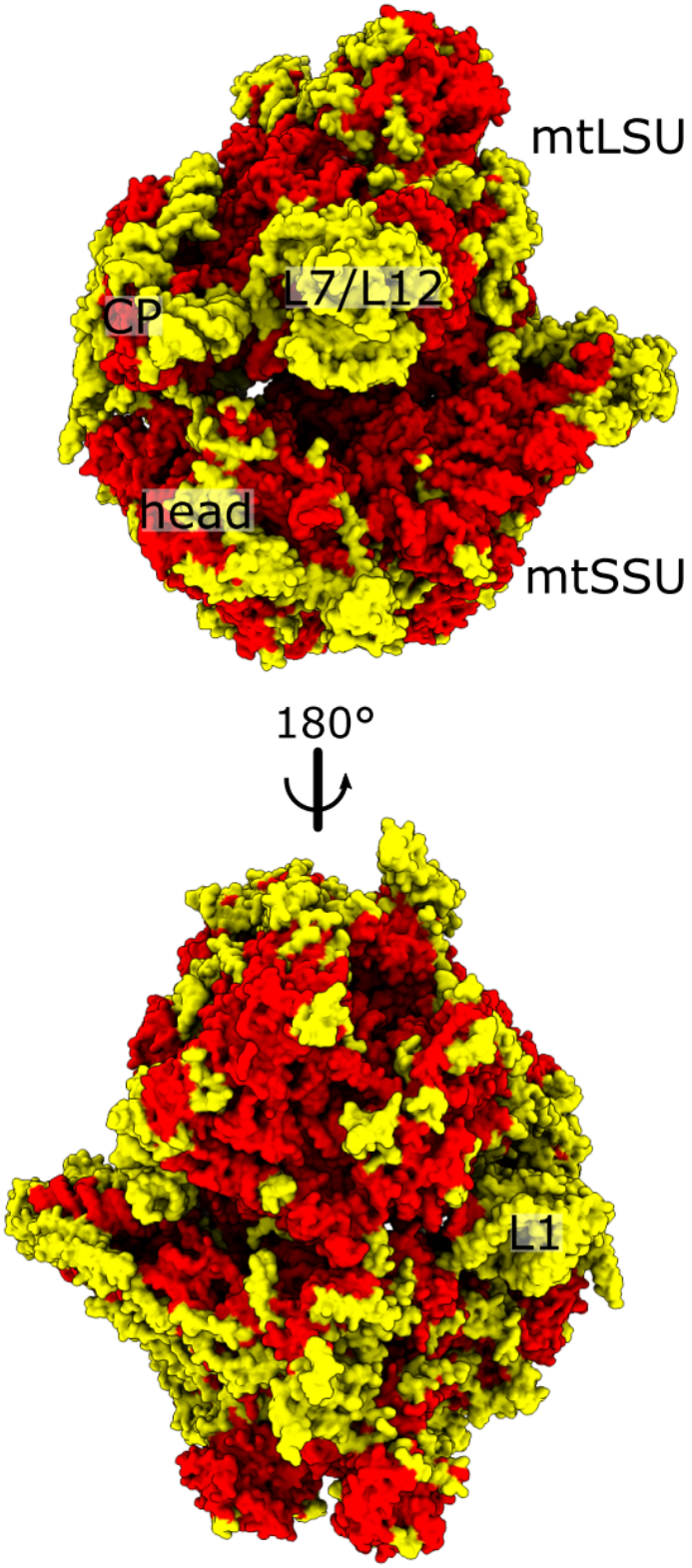

Appendix Figure S9. Improvements in the fungal mitoribosomal model. The newly modeled and improved features in the current structure (yellow) compared with the previous model (red) of the *S. cerevisiae* mitoribosome (PDB ID: 5MRC).

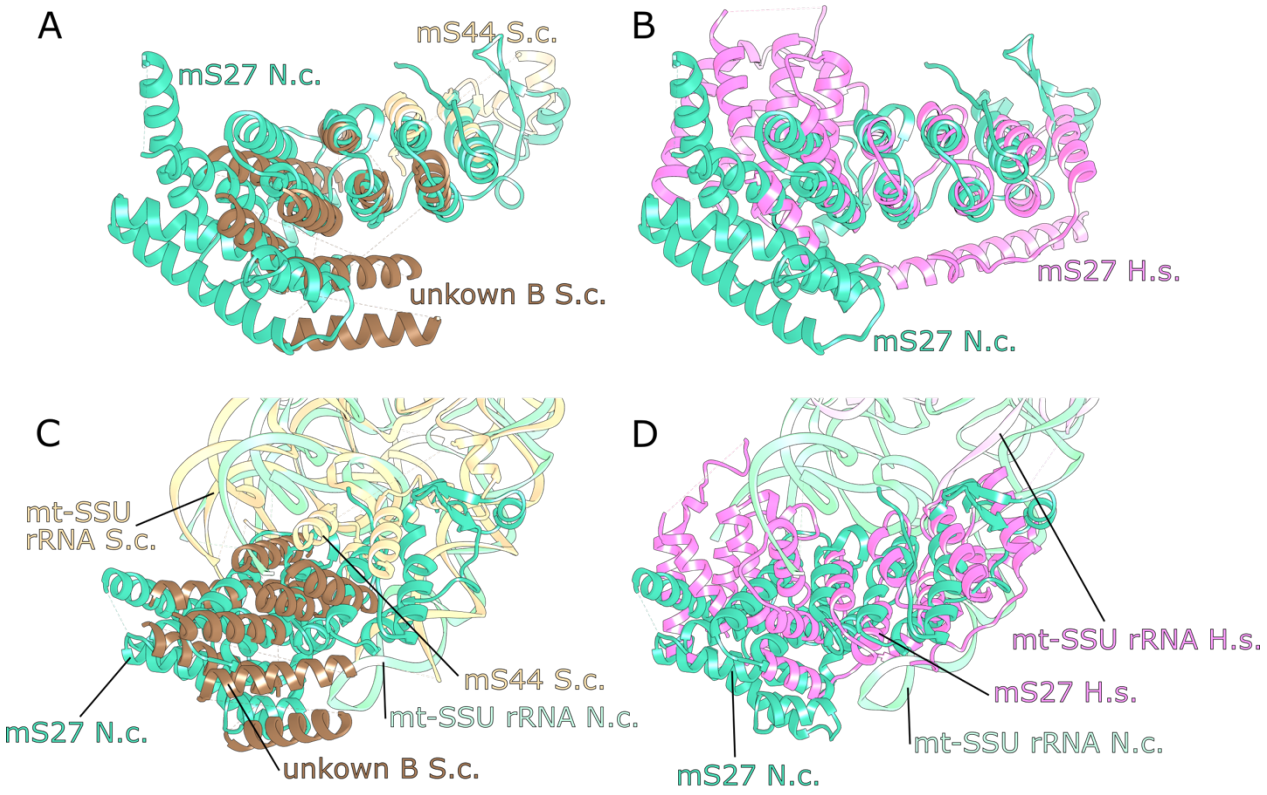

Appendix Figure S10. Superposition of mS27 orthologs. (A) *N. crassa* and *S. cerevisiae* mS27 is superimposed (previously assigned as mS44, 'unknown B'). (B) *N. crassa* and *H. sapiens* mS27 is superimposed, showing similar fold. (C) Superposition based on mtSSU rRNA suggests the same location form mS27 from *N. crassa* and *S. cerevisiae*. (D) Superposition based on mtSSU rRNA suggests the same location form mS27 from *N. crassa* and *H. sapiens.*

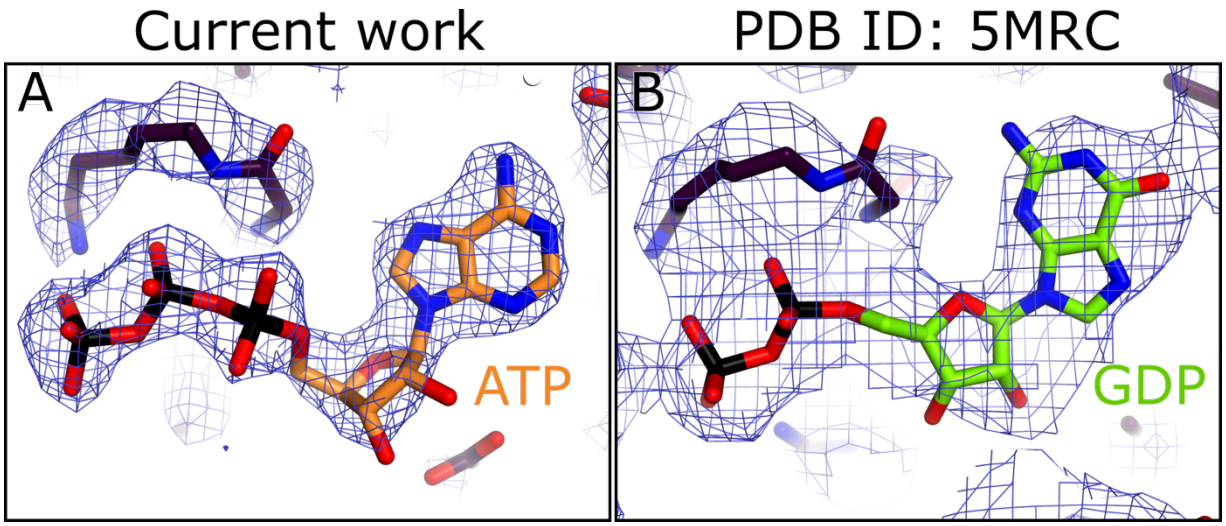

Appendix Figure S11. Comparison of the nucleotide density for mS29 between the current model of *N. crassa* and previous work. (A) The density for ATP bound to mS29 in the current work with the corresponding model (B) For comparison the density of the previously modeled GDP in *S. cerevisiae* is shown.

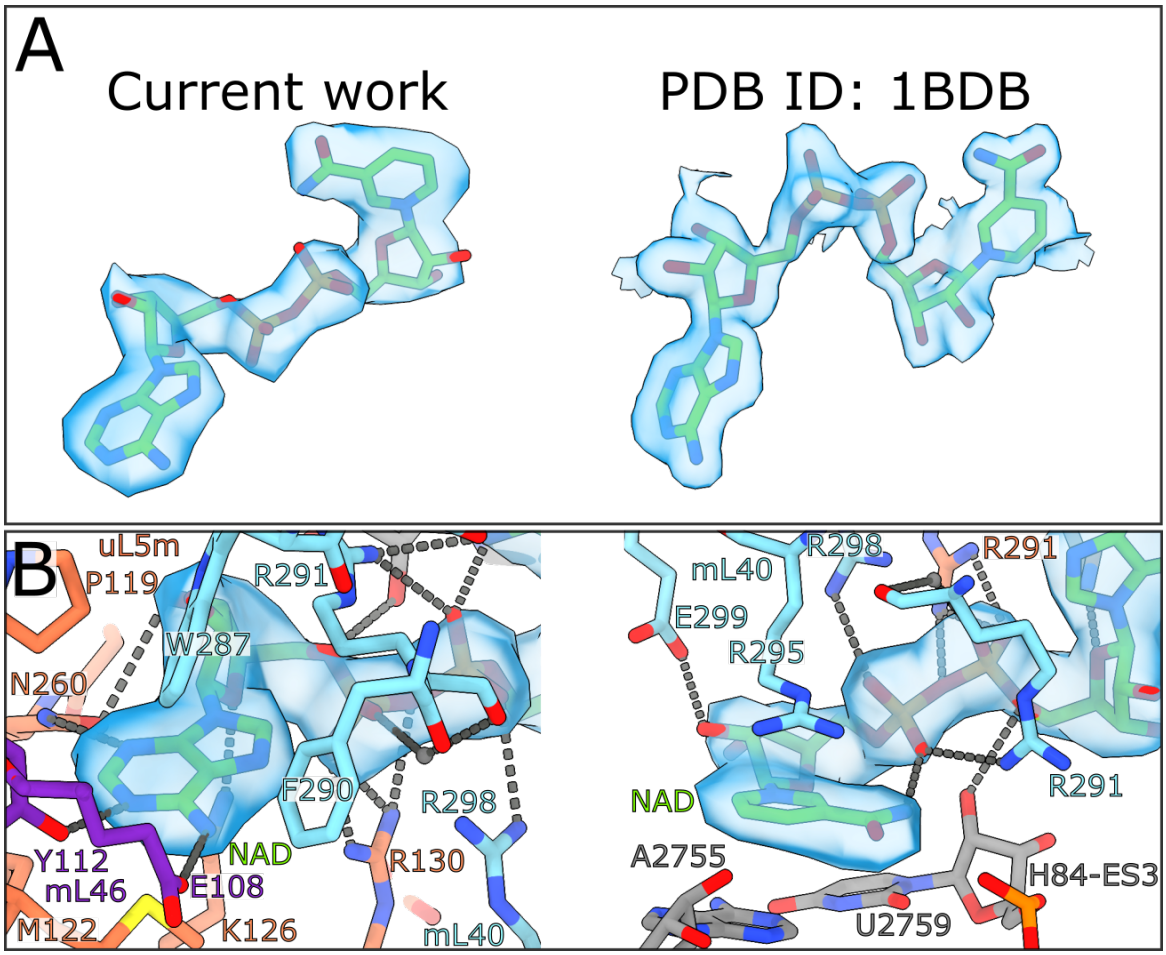

Appendix Figure S12. Density map and interactions of the NAD binding pocket in the CP of *N. crassa.* (A) Comparison of the density in the current work with 2 Å resolution crystal structure confirms the correct assignment of NAD in the model. Both studies show the nicotine amid in syn-conformation. (B) Interactions formed by NAD with uL5, mL40 and H84-ES3 rRNA showed from two opposite views. One view is centered on the adenine ring and the other view around the nicotine amid. Hydrogen bonds and charged interactions are indicated by black dashed lines. Residues and nucleotides are colored and labeled correspondingly.

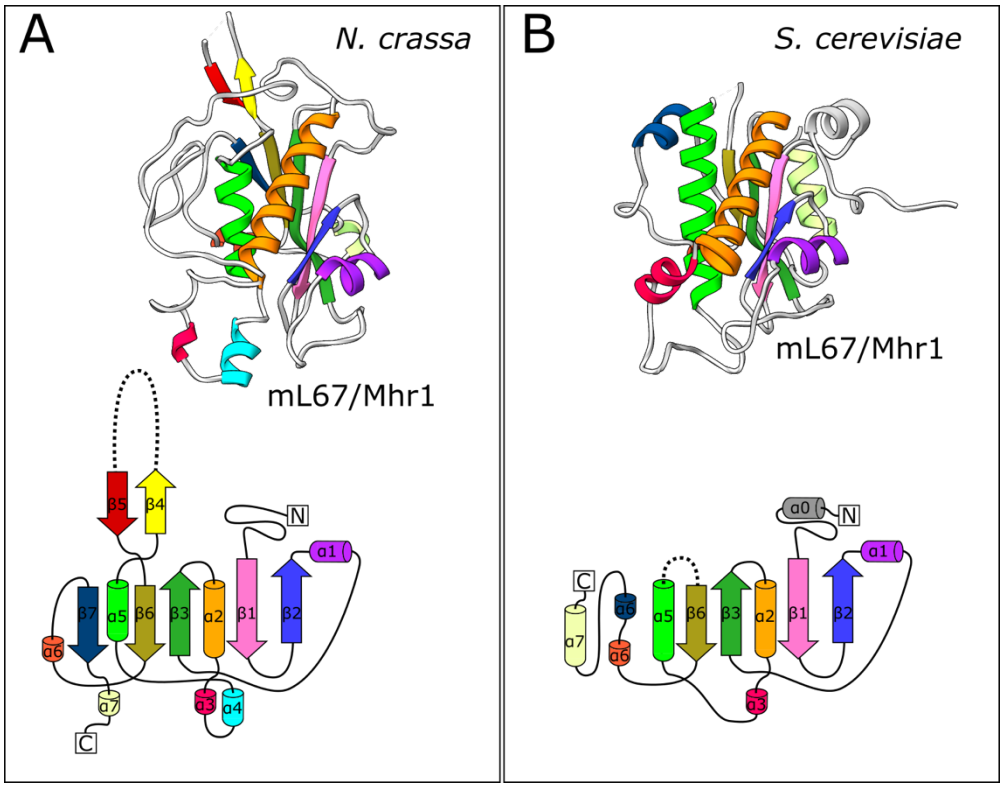

783

784 **Appendix Fig S13. Structure and topology of mL67/Mhr1.** (A) Three dimensional model and
785 topology of *N. crassa* mL67/Mhr1 with secondary structure elements colored. The specific
786 extension between β-strands 4 and 5 is indicated as dashed line. (B) Three dimensional model and
787 topology of *S. cerevisiae* mL67/Mhr1 following the same color scheme in panel A.
788

789 **Appendix Table S1. Data and model statistics.**

Data collection	**mtLSU**	**mtSSU**	**Monosome with E-site tRNA**	**Monosome with P-site tRNA**	**Monosome with tRNA in P/E state**	**Late stage intermediate mtLSU (Atp25)**
Microscope	Titan Krios	Titan Krios	Titan Krios	Titan Krios	Titan Krios	Titan Krios
Detector	K2 Summit	K2 Summit	K2 Summit	K2 Summit	K2 Summit	K2 Summit
Magnification	130,000	130,000	130,000	130,000	130,000	130,000
Voltage [kV]	300	300	300	300	300	300
Total electron dose [e^{-}/Å^2]	35	35	35	35	35	35
Defocus range [μm]	−0.8 to −3.0	−0.8 to −3.0	−0.8 to −3.0	−0.8 to −3.0	−0.8 to −3.0	−0.8 to −3.0
Pixel size [Å]	1.06	1.06	1.06	1.06	1.06	1.06
Final particles	131,806	131,806	23,802	24,611	37,908	24,142
Resolution [Å] (overall/ LSU core / LSU CP / LSU L10 region / LSU L1 stalk / SSU head / SSU body / SSU tail)	2.74/2.70/2.88/3.03/3.48/-/-/-t	2.85/-/-/-/-/2.79/2.79/2.88	3.10/2.99/3.14/3.50/-/3.14/ 3.07/3.21	3.05/2.97/3.01/ 3.07/-/3.03/ 3.03/3.10	2.99/2.90/3.12/ 3.14/3.48/2.94/ 2.94/3.05	3.03/-/-/-/-/-/-/-
Map-sharpening *B* factor [Å^2] (overall/ LSU core / LSU CP / LSU L10 region / LSU L1 stalk / SSU head / SSU body / SSU tail)	-50.7/-48.3/-69.6/-74.4 /-66.7/-/-/-	-51.4/-/-/-/-/-48.3/-56.5/-64.7	-41.2/-33.6/ -60.9/-55.2/-/ -50.4/-32.3/ -55.4	-49.0/-36.8/ -46.0/-56.2/-/ -50.1/-50.1/ -57.0	-45.8/-46.1/ -55.9/-55.9/ -66.7/-41.1/ -45.8/-61.0	-40.3/-/-/-/-/-/-/-
Model composition						
Total atoms (non-hydrogen/ hydrogen)	223,408/97,527	167,560/76,668	390,797/173,689	392419/174345	394,205/175,280	207,611/91,129
Chains (RNA/ protein)	1/44	1/37	3/78	4//79	4/80	1/42
RNA residues	2820	1435	4334	4362	4357	2529
Protein residues	8200	7528	15553	15604	15727	7802
Metal ions (Mg^{2+}/ K^{+}/ Zn^{2+})	163/12/2	97/22/0	249/50/2	250/49/2	242/55/2	144/23/2
Ligands (ATP/ NAD/ spermine)	0/1/1	1/0/0	1/1//1	1/1/1	1/1/1	0/1/1
Refinement						
Model to map CC (CC_{mask}/ CC_{bo}-/ CC_{peaks}/ CC_{volume})	0.84/0.74/0.71/0.82	0.86/0.72/0.66/0.84	0.81/0.77/0.75/0.80	0.83/0.78/0.77/0.82	0.84/0.79/0.78/0.83	0.81/0.76/0.74/0.79
Average *B* factor [Å^2] (protein/RNA/ metal ion and ligand/)	172.29/170.34/75.62	95.19/121.44/36.55	117.81/173.91/83.19	56.92/82.51/38.83	69.33/102.72/29.15	68.65/131.13/25.77
RMSD bond lengths [Å]	0.002	0.002	0.002	0.002	0.002	0.002
RMSD bond angles [°]	0.382	0.357	0.373	0.354	0.362	0.402
Validation by MolProbity						
Clash score	1.57	2.48	1.86	1.75	1.69	1.61

Rotamer outliers [%]	0.23	0.14	0.69	0.41	0.71	0.74
Ramachandran plot [%] (Favored/ allowed/ disallowed)	98.31/1.69/0.00	98.40/1.60/0.00	98.21/1.76/0.03	98.44/1.53/0.03	98.20/1.79/0.01	98.44/1.56/0.00
EMDB ID (overall/ LSU core / LSU CP / LSU L10 region / LSU L1 stalk / SSU head / SSU body / SSU tail)	10973/10974/ 10976/10975/-/-/-/-	10958/-/-//-/-/ 10961/10962/ 10963	10978/10979/10981/ 10980/-/10982/ 10984/10983	10985/10986/10989/ 10988/-/10990/ 10991/10992	10965/10966/10968/ 10967/10971/10969/ 10970/10972	10977/-/-/-/-/-/-/-
PDB ID	6YWS	6YW5	6YWX	6YWY	6YWE	6YWV

792 **Appendix Table S2. List of RNA and proteins from mtLSU.**

Name	Gene	Uniprot ID	Chain ID	Modeled	Size	Notes
23S rRNA	–	–	A	2820	3464	Spermine bound next to A1271.
uL1m	MRPL1	Q1K699	e	59–300	303	Conserved in *S. cerevisiae* and human but disordered in their structures.
uL2m	RML2	Q7SCX7	B	54–379	383	Likewise its *S. cerevisiae* counterpart, NT extension locates at the subunits interface.
uL3m	MRPL9	Q1K8T6	C	63–369	384	A helix at CT extension is similar to the human uL3m. This extension does not exist in the *S. cerevisiae* counterpart.
uL4m	YML6	V5IMN1	D	62–302, 312–324	325	
uL5m	MRPL7	Q1K6P0	E	44–352	352	
uL6m	MRPL6	Q7RZF0	F	52–252	255	
bL9m	MRPL50	Q7S054	G	52–125	300	
uL10m	MRPL11	Q7RZ62	f	54–298	347	Conserved in *S. cerevisiae* and human. It is not modeled in the *S. cerevisiae* structures.
uL11m	MRPL19	Q7RX40	g	12–158	158	Conserved in *S. cerevisiae* and human. It is not modeled in the *S. cerevisiae* structures.
uL13m	MRPL23	Q7SBV6	H	1–183	183	
uL14m	MRPL38	Q7SBJ8	I	1–46, 59–131	131	
uL15m	MRPL10	Q7SB98	J	47–289	312	
uL16m	MRPL16	F5HIJ5	K	61–228	249	
uL17m	MRPL8	Q1K8C8	L	2–193	193	CT extension unlike its *S. cerevisiae* counterpart lacking a helix.
bL19m	IMG1	Q7RYW8	M	41–234	258	
bL21m	MRPL49	Q7SGE5	N	85–217	217	
uL22m	MRPL22	Q7S5N0	O	43–71, 122–364	364	NT extension extensively remodeled with respect to its *S. cerevisiae* counterpart, whereas CT extension is quite similar. NT partially occupies the position of the absent bacterial rRNA helix 24.
uL23m	MRP20	Q7SA60	P	13–192	228	CT extension remodeled respective to its *S. cerevisiae* counterpart.
uL24m	MRPL40	Q7RXU7	Q	1–353	396	NT extension is a long helix that is not like its bacterial, *S. cerevisiae*, and human counterparts. CT extension is similar to that of the *S. cerevisiae*; it covers a long distance through the surface thereby connecting different parts of the large subunit. The CT extension compensates the absence of bacterial helices 15 and 16.
bL27m	MRP7	Q1K730	R	67–196, 248–383	447	NT extension is similar to bacterial, *S. cerevisiae* and human counterparts. CT extension extensively remodeled respective to *S. cerevisiae* bL27m, and partially interacts with rRNA helix 82.
bL28m	MRPL24	Q7SC44	S	42–203, 209–225	274	CT extension remodeled extensively respective to *S. cerevisiae* counterpart.
uL29m	MRPL4	Q7S910	T	44–223	263	
uL30m	MRPL33	Q1K8Y7	U	2–102, 125–161	161	
bL31m	MRPL36	Q1K7L7	V	48–128, 189–207	219	Bridging the mtLSU CP and the mtSSU head.
bL32m	MRPL32	Q1K4P1	W	64–122	129	Zn ion coordination.
bL33m	MRPL39	V5IM60	X	7–54	59	
bL34m	MRPL34	Q96U95	Y	95–140	140	
bL36m	RTC6	Q7S4E7	0	79–124	124	Zn binding

mL38	MRPL35	Q7RXV8	1	83–449	449	CT extension partially compensates the absence of bL35. Stabilizes helices 84-ES and 82-ES.
mL40	MRPL28	V5IQE0	2	248–370	370	Stabilize helices 82-ES, 84-ES, 38-ES1. NAD is binding and interacting with mL40.
mL41	MRPL27	Q7S5W0	3	9–103	103	
mL43	MRPL51	Q7S300	4	2–138	138	
mL44	MRPL3	Q7SA88	5	55–237, 273–439	439	NT extension slightly remodeled respective to *S. cerevisiae* mL44. CT extension interacts with helix 0-ES1. It forms heterodimer with mL57.
mL46	MRPL17	Q7S1Z3	6	82–245 253–303 311–368	368	Interacts with helices 38-ES1 and 82-ES.
mL49	IMG2	Q7S518	7	82–165	165	Most likely interacts with helix 28.
mL50	MRPL13	Q7S711	8	112–442	443	Extensively remodeled. A 31 amino-acid long helix at the solvent-exposed surface of the protein. Interacting with helices 45 and 46.
mL53	MRPL44	Q7SGH0	h	1–98	98	Conserved in *S. cerevisiae* and human. It is not modeled in the *S. cerevisiae* structures.
mL54	MRPL37	Q7SCZ3	i	77–118, 137–218	218	Bridges L10/L11 area to CP. Conserved in *S. cerevisiae* and human. It is not modeled in the *S. cerevisiae* structures and only one helix is modeled in the human structures.
mL57	MRPL15	Q7S1R6	9	61–266	267	Forms a heterodimer with mL44. Stabilizes helix 0-ES1.
mL58	MRPL20	Q1K6U7	a	41–103, 128–225	225	Interacts with helix 0.
mL59	MRPL25	A0A0B0DMU6	b	2–162	162	
mL60	MRPL31	U9W8F2	c	13–110	110	
mL67	MHR1	Q7RYM5	d	33–218 243–291	292	Similar to its *S. cerevisiae* counterpart with slight remodeling at NT and CT extensions.
mL108	MRPL49	Q7RWZ7	j	2-196	201	Conserved but not modeled in *S. cerevisiae*.
Nascent polypeptide	–	–	cc	7		

793

794 **Appendix Table S3. List of RNA and proteins from mtSSU.**

MRP	Gene	Uniprot ID	Chain ID	Modeled	Size	Notes
16S rRNA	–	–	aa	1435	1864	
bS1m	MRP51	A7UWX2	AA	5–124, 132–213, 229–269, 288–337, 341–358, 368–430	470	
uS2m	MRP4	V5ILE0	BB	107–396	428	
uS3m	VAR1	P23351	CC	17–171, 193–369, 403–508	508	
uS4m	NAM9	Q7SA90	DD	1–215, 379–453	453	
uS5m	MRPS5	Q1K548	EE	56–180, 236–477	477	Has a unique insertion to form a unique second beak.
bS6m	MRP17	Q7SB95	FF	1–117	117	
uS7m	RSM7	Q7S6M9	GG	87–309	309	
uS8m	MRPS8	Q7SHF3	HH	2–161	161	
uS9m	MRPS9	Q7S7R6	II	69–315	315	
uS10m	RSM10	Q7RYL4	JJ	81–268	268	
uS11m	MRPS18	Q7SGU0	KK	253–376	376	
uS12m	MRPS12	Q7S9I4	LL	45–172	174	
uS13m	SWS2	Q7S2C2	MM	2–119	119	
uS14m	MRP2	Q7SF85	NN	2–113	113	
uS15m	MRPS28	Q1K5G1	OO	38–106, 114–320	320	
bS16m	MRPS16	P08580	PP	2–99	107	
uS17m	MRPS17	Q7S4E0	QQ	6–163	165	A unique C–terminal helix, which binds the IF_1 dimer.
bS18m	RSM18	Q1K8E0	RR	108–241	256	
uS19m	RSM19	Q1K8V2	SS	9–89	91	
bS21m	MRP21	Q7SAJ1	TT	149–236	236	
mS23	RSM25	F8MRK5	UU	2–128, 142–238	240	
mS26	PET123	Q7SHR9	VV	47–257, 262–287, 293–316	316	

mS27	MRP13	Q7RYW7	WW	40–270, 275–396	396	Corresponds to mS27 in human. *S. cerevisiae* mS44 and the unknown B (PDB ID: 5MRC) are one connected protein, which corresponds to human and *N. crassa* mS27.
mS29	RSM23 /DAP3	Q7SD06	XX	57–66, 72–469	469	DAP3 death associated protein 3. ATP and Mg ion are bound.
mS33	RSM27	Q1K5R0	YY	2–100	108	
mS35	RSM24	Q1K5Z0	ZZ	42–353	382	Has a unique N–terminal domain to form a unique beak.
mS37	MRP10	Q7S4Y4	11	2–89	90	
mS38	COX24	Q7SHR6	22	312–344	344	
mS41	FYV4	Q1K6Q3	33	43–235	236	
mS42	RSM27 /MRP1	Q7S2H6	44, 55	43–302	310	Homolog of Fe superoxide dismutase. Lost the catalytic Fe ion binding side. Two chains form a homodimer, in contrast to the mS42-mS43 heterodimer in *S. cerevisiae*.
mS45	MRPS35	Q7SHB2	66	66–348	348	
mS46	RSM28	Q7SG49	77	223–401	414	
mS47	MRP5 /EHD3	Q1K7A4	88	42–508	508	3-hydroxyisobutyryl-CoA hydrolase. Probably an active enzyme because its active site is conserved.
ATP–IF_1	INH1	V5IRA3	00, 99	39–86	95	ATP synthase inhibitor 1. Forms a homodimer located in the mtSSU tail region.
tRNA	–	–	bb	73		P, E or P/E tRNA state. The density is an average of different tRNA species.
mRNA	–	–	ee	11		mRNA in the P and P/E state. The density is an average of different mRNAs.

795

Appendix Table S4. List of detected proteins from the mass spectrometry. 245 detected proteins are sorted by the score. 203 proteins show a higher score than 4. Mitoribosomal and cytosolic ribosomal proteins are colored green and blue, respectively. Pyruvate dehydrogenase complex components and related proteins are colored orange. mS27, mL108, IF_1, and Atp25 are highlighted as yellow. bL33m, bL34m, mS37 were not detected.

	Uniprot code	Protein name	Score	#PSMs	#Unique peptides	#Peptides	Coverage	Protein length (aa)
1	P20285	Dihydrolipoyl transacetylase (E2)	8482.07	1838	31	31	71.40	458
2	A0A0B0DH36	Dihydrolipoyl dehydrogenase (E3)	6507.81	1565	31	31	69.51	528
3	Q7RYJ2	Pyruvate dehydrogenase E1 subunit alpha	5394.65	1125	24	24	58.99	417
4	Q1K937	Pyruvate dehydrogenase E1 subunit beta	4718.08	1130	18	18	63.85	379
5	Q7RWS2	Pyruvate dehydrogenase X component	1590.71	310	24	24	53.29	426
6	Q1K730	bL27m	1182.96	263	10	10	23.94	447
7	Q7SCC3	Pyruvate dehydrogenase kinase	1076.15	260	26	26	70.94	437
8	A7UWX2	bS1m	955.13	186	24	24	60.64	470
9	Q1K7A4	mS47	909.98	224	22	22	48.62	508
10	Q7RYW7	mS27	886.51	245	18	18	51.77	396
11	Q7S1Z3	mL46	877.63	216	13	13	46.20	368
12	V5ILE0	uS2m	868.08	189	14	14	50.00	428
13	Q1K6P0	uL5m	794.87	230	12	12	40.34	352
14	A0A0B0DWL0	mS29	772.02	191	17	17	44.35	469
15	Q7S7R6	uS9m	768.41	191	11	11	44.13	315
16	Q1K548	uS5m	767.75	192	19	19	51.36	477
17	Q7SA88	mL44	727.28	169	12	12	43.28	439
18	V5IPE9	uL4m (long variant)	721.36	179	2	14	49.00	349
19	Q7S4E0	uS17m	698.39	172	7	7	55.76	165
20	Q7S2H6	mS42	685.74	165	11	11	48.71	310
21	Q7RXU7	uL24m	675.77	177	21	21	62.12	396
22	Q7RYM5	mL67	665.01	156	16	16	41.44	292
23	A0A0B0DKG3	mS23	662.93	184	13	13	60.00	240
24	Q7SAJ1	bS21m	636.34	166	4	4	44.92	236
25	Q7S711	mL50	610.06	148	16	16	44.02	443
26	V5IMN1	uL4m (short variant)	609.44	159	1	13	46.15	325
27	Q1K5G1	uS15m	597.54	149	10	10	45.63	320
28	Q7SA90	uS4m	579.85	136	23	23	45.25	453
29	Q1K5Z0	mS35	577.84	151	22	22	52.88	382
30	Q7SHR9	mS26	558.82	158	17	17	52.85	316
31	Q7RZF0	uL6m	551.88	154	10	10	43.92	255
32	Q7SC44	bL28m	547.46	136	16	16	52.55	274
33	Q6MW06	mL38	526.05	137	20	20	56.51	407
34	P23351	uS3m	509.81	143	16	16	37.20	508
35	Q1K8T6	uL3m	498.70	124	15	15	49.48	384
36	Q1K699	uL1m	468.76	113	7	7	33.99	303
37	Q7S5N0	uL22m	440.56	110	13	13	31.04	364
38	Q7SB95	bS6m	426.08	118	3	3	26.50	117
39	Q1K8Y7	uL30m	418.77	134	8	8	44.72	161
40	Q7SG49	mS46	405.15	105	17	17	47.10	414

41	Q7S1R6	mL57	390.66	95	10	10	38.20	267
42	Q7SB98	uL15m	385.21	105	10	10	32.05	312
43	Q7RZ62	uL10m	381.44	97	14	14	47.26	347
44	Q7RWZ7	mL108	378.36	72	8	8	38.31	201
45	F5HIJ5	uL16m	361.85	103	10	10	41.37	249
46	Q1K6U7	mL58	305.71	62	6	6	40.44	225
47	Q7RYW8	bL19m	294.51	87	9	9	42.64	258
48	Q7S910	uL29m	282.58	74	10	10	30.80	263
49	Q7SBV6	uL13m	274.62	74	6	6	46.99	183
50	Q1K8E0	bS18m	271.53	72	8	8	42.97	256
51	Q7RYL4	uS10m	271.22	75	9	9	40.30	268
52	Q7SA60	uL23m	248.66	62	10	10	56.58	228
53	Q1K6Q3	mS41	246.19	61	7	7	27.12	236
54	Q7RYV0	bL12m	245.65	70	6	6	51.70	176
55	A0A0B0DMU6	mL59	245.02	54	8	8	40.12	162
56	A0A0B0DK80	bL9m	243.33	79	10	10	39.67	300
57	Q7SHB2	mS45	226.54	68	13	13	32.18	348
58	Q7SGU0	uS11m	217.99	52	6	6	18.62	376
59	Q7SCX7	uL2m	212.12	54	11	11	34.99	383
60	Q7SCZ3	mL54	201.56	49	8	8	36.24	218
61	Q7SI52	Rsm22	200.22	53	22	22	37.82	870
62	Q7S6M9	uS7m	199.91	64	8	8	29.45	309
63	Q1K7L7	bL31m	180.52	31	5	5	35.62	219
64	Q7SGE5	bL21m	170.97	41	5	5	45.16	217
65	Q7S300	mL43	167.81	43	6	6	47.10	138
66	Q7S518	mL49	166.34	48	5	5	16.36	165
67	Q7SHF3	uS8m	158.39	34	6	6	42.24	161
68	Q1K7B7	uL4	134.60	29	11	11	36.57	361
69	Q6MVY0	uS13m	134.41	30	2	2	28.57	119
70	Q7RX40	uL11m	128.45	32	7	7	49.37	158
71	Q7RVX2	Hsp70-like protein	126.53	31	17	17	27.54	668
72	Q7SE03	uS4	125.66	35	9	9	41.00	261
73	P59671	uL3	124.48	35	9	9	20.92	392
74	Q1K8C8	uL17m	119.78	31	6	6	30.05	193
75	P07038	Plasma membrane ATPase	114.18	30	13	13	19.46	920
76	Q7SGE3	Ribosomal protein P1/P2	110.07	23	6	7	78.18	110
77	Q1K6B1	T-box family protein	105.90	29	11	11	14.00	1150
78	Q1K5R0	mS33	100.29	22	4	4	47.22	108
79	Q7S5S5	Stomatin family protein	98.23	26	7	7	25.75	431
80	U9W8F2	mL60	93.81	26	3	3	26.36	110
81	A0A0B0DYT5	uS11	91.90	20	7	7	52.00	150
82	P08580	bS16m	87.87	25	4	4	52.34	107
83	Q7S5W0	mL41	86.96	23	4	4	40.78	103
84	Q7SBJ8	uL14m	86.85	25	3	3	27.48	131
85	Q7S9I4	uS12m	85.28	24	2	2	18.97	174
86	Q7RV52	uS3	82.20	25	7	7	35.11	262

87	Q6MFL6	eL8	81.44	22	8	8	30.92	262
88	Q9P5N9	Oxoglutarate dehydrogenase (E1)	78.87	18	9	9	13.89	1087
89	V5IRA3	IF_1	78.64	26	3	3	32.63	95
90	Q7SGA6	uL6	76.60	26	9	9	41.45	193
91	A0A0B0E4N1	eL13	75.26	19	7	7	34.11	214
92	Q7RXY1	eL32	75.24	21	4	4	29.01	131
93	O59953	uL18	74.66	17	7	7	35.55	301
94	Q01291	uS2	71.21	19	3	3	8.62	290
95	Q872B4	Pentatricopeptide repeat protein (uncharacterized)	67.63	18	10	10	19.52	753
96	V5IQE0	mL40	67.21	20	2	2	14.36	202
97	A0A0B0E325	uS5	66.50	17	5	5	22.81	263
98	Q1K7X3	Elongation factor Tu	64.12	15	7	7	24.26	437
99	Q7S8I8	Uncharacterized protein	61.27	16	10	10	16.48	1044
100	V5IQ82	eS6	60.03	16	5	5	29.33	208
101	Q871N9	eS1	59.99	15	7	7	26.17	256
102	P87224	CoxI translation protein Cya5	59.58	16	13	13	16.55	1136
103	A0A0B0E3A4	Pentatricopeptide repeat protein (uncharacterized)	59.57	14	11	11	20.24	830
104	P08978	uL15	59.50	17	6	6	45.64	149
105	A0A0B0DXR5	Band 7 like (uncharacterized)	56.23	15	9	9	23.05	525
106	Q7RV75	uS8	54.28	11	2	2	23.08	130
107	Q7SH25	Dihydrolipoamide acetyltransferase	50.62	14	9	9	22.24	562
108	Q7S5N9	eL19	49.20	14	7	7	30.73	192
109	Q7SER1	6-phosphogluconate dehydrogenase like (uncharactarized)	48.25	12	6	6	18.73	550
110	Q9HDH1	AAA protease IAP-1	47.79	11	5	5	11.38	738
111	Q7S7F1	eL30	46.14	12	3	3	28.44	109
112	A0A0B0DSS5	Atp25	45.93	11	4	4	12.20	492
113	Q7S796	Ribosomal protein P1/P2	43.73	8	3	4	60.55	109
114	Q96TJ5	uL10	41.47	11	7	7	38.98	313
115	Q7RZS0	uL1	41.31	10	4	4	24.88	217
116	P27770	eS17	40.74	11	4	4	41.10	146
117	Q7SBD5	uL30	40.26	11	4	4	24.19	248
118	Q1K580	eL27	40.22	11	3	3	28.89	135
119	Q9P4Z0	eS8	38.84	11	3	3	21.29	202
120	A0A0B0E8U3	Asc1/Rack1	37.47	11	5	5	18.04	316
121	Q7SFZ2	uS17	36.65	9	1	2	8.70	161
122	Q7SBS9	uL23	33.46	9	3	3	17.95	156
123	V5IKF9	RF-1 (uncharacterized)	32.58	9	5	5	28.57	203
124	A0A0B0DDI8	Dihydrolipoamide succinyltransferase	32.13	9	4	4	15.37	423
125	V5IQT8	eL20	31.75	10	2	2	16.09	174
126	Q1K4V7	uL24	31.25	8	3	3	25.74	136
127	O43105	eS7	30.46	6	3	3	23.76	202

128	Q7RXJ4	eL18	30.09	5	2	2	22.40	183
129	Q1K6Y9	Inositol-3-phosphate synthase	29.95	10	1	1	7.26	537
130	O93798	eS21	29.72	7	1	1	18.39	87
131	Q7SBR1	RNA helicase mrh4	29.70	9	8	8	18.40	625
132	Q9C285	uL11	28.80	8	4	4	35.76	165
133	P23704	ATP synthase subunit beta	28.62	8	8	8	25.63	519
134	F5HE85	eS10	27.86	8	4	4	26.99	163
135	Q7SGH0	mL53	25.87	8	2	2	23.47	98
136	Q7SBD8	eS19	25.46	8	2	2	16.11	149
137	A0A0B0DRF2	uS7	25.29	9	4	4	21.13	213
138	Q7SH34	HMG-box protein (uncharacterized)	25.10	7	5	5	20.68	324
139	Q2WEG9	eL6	25.09	7	2	2	26.89	119
140	Q1K526	Pentatricopeptide repeat protein (uncharacterized)	24.35	7	6	6	12.09	761
141	Q7S156	eL33	24.21	6	1	1	14.68	109
142	P12063	TyrRS, mitochondrial	23.90	7	7	7	14.05	669
143	Q7RVQ9	uL2	23.37	5	2	2	18.11	254
144	Q7RXX0	uS13	22.86	6	3	3	20.51	156
145	V5IRR9	RRM domain containing protein (uncharacterized)	22.62	7	3	3	12.21	344
146	Q7S1Z1	eL43	22.14	5	1	1	19.57	92
147	P47950	RNase cyt-4	20.35	5	4	4	7.34	1117
148	Q6MVD1	Inner membrane mitoribosome receptor Mba1	19.97	5	3	3	18.15	281
149	Q7SGF1	uS19	19.78	5	2	2	23.03	152
150	Q7S5B6	Uncharacterized protein	19.41	5	3	3	5.32	959
151	Q1K5V9	eS24	18.78	5	2	2	11.76	136
152	Q7SF85	uS14m	18.68	6	1	1	10.62	113
153	Q7SDJ3	Dynamin	18.62	5	5	5	11.24	801
154	Q9C2B9	eL38	18.61	6	1	1	17.50	80
155	Q7SEP1	eL36	18.37	4	1	1	13.46	104
156	Q7RW06	Hsp70	17.81	5	4	5	12.14	585
157	Q96U90	uS19m	17.06	4	2	2	35.00	80

158	Q7S6W5	eS28	16.36	5	2	2	23.53	68
159	Q871K5	SPS2 (uncharacterized)	16.09	5	3	3	10.95	411
160	Q9C2H9	MetRS, mitochondrial	16.02	4	4	4	11.41	622
161	Q7S8Z8	Obg	15.81	4	4	4	11.17	591
162	Q7SDH0	uS15	14.84	5	4	4	33.77	151
163	Q1K6R7	Band-7 family protein (uncharacterized)	14.59	4	3	3	16.30	276
164	Q7S3G1	uS10	14.18	5	2	2	17.09	117
165	P21772	eS26	14.14	4	1	1	12.61	119
166	Q7RV74	eS12	13.92	5	2	2	13.61	147
167	Q7SH55	TPR-like (uncharacterized)	12.83	4	3	3	4.68	833
168	Q7SFJ9	uS9	12.71	4	2	2	18.31	142
169	Q7S663	FAD/NAD-binding protein (uncharacterized)	12.64	3	3	3	12.23	458
170	Q9HE25	uL22	11.82	4	3	3	15.05	186
171	Q9HE83	Phosphate transport protein MIR1	11.52	3	2	2	8.78	319
172	P37211	ATP synthase subunit alpha	11.33	3	3	3	7.44	551
173	Q7S5Z0	2-oxoisovalerate dehydrogenase subunit alpha	11.32	3	3	3	11.73	469
174	Q7SDU2	eL24	11.15	4	1	1	7.05	156
175	Q7RVN0	uL5	10.97	3	1	1	8.05	174
176	Q7S237	Uncharacterized protein	10.47	3	3	3	10.61	424
177	Q8X034	eL15	10.26	3	2	2	12.81	203
178	Q2WEG7	uL14	10.24	3	2	2	27.38	84
179	Q870U1	RF-1 like	10.19	2	2	2	8.84	430
180	Q7RWM8	EngB like	9.70	3	2	2	6.75	504
181	P22572	Carbamoyl-phosphate synthase arg-2	9.65	3	3	3	14.79	453
182	Q7S1D6	Malate dehydrogenase	9.53	3	3	3	10.42	336
183	Q9P720	uL13	9.42	3	2	2	6.93	202
184	Q7SC06	eS25	9.05	3	1	1	10.31	97
185	Q7S8N1	Protein kinase-44	8.89	3	1	1	3.24	1267
186	Q7SDQ6	Atg14 (uncharacterized)	8.77	3	1	1	5.34	731
187	Q7SHR6	mS38	8.41	2	2	2	10.17	344

188	**Q7SI18**	**eL14**	**8.27**	**3**	**1**	**1**	**7.04**	**142**
189	**Q7S731**	**RNA methyltransferase (uncharacterized)**	**7.93**	**2**	**1**	**1**	**2.17**	**644**
190	**R4H4I1**	**PPM-type phosphatase**	**7.73**	**2**	**2**	**2**	**6.04**	**563**
191	**Q7S9T5**	**RNA helicase Suv3**	**7.00**	**2**	**2**	**2**	**3.27**	**796**
192	**P15181**	**LeuRS, mitochondrial**	**6.85**	**2**	**2**	**2**	**4.12**	**994**
193	**Q7SG89**	**Glycine cleavage system P protein**	**6.73**	**2**	**2**	**2**	**2.09**	**1100**
194	**Q6M978**	**Glutathione Transferase like**	**6.28**	**2**	**1**	**1**	**8.38**	**346**
195	**P24918**	**Complex I, NDUFS1**	**6.26**	**2**	**2**	**2**	**3.90**	**744**
196	**Q1K5Z8**	**2-oxoisovalerate dehydrogenase subunit beta**	**6.00**	**2**	**2**	**2**	**7.19**	**417**
197	**P54898**	**Arg-6, mitochondrial**	**5.89**	**2**	**2**	**2**	**2.64**	**871**
198	**Q1K6Z3**	**eL22**	**5.57**	**1**	**1**	**1**	**16.67**	**126**
199	**Q7S625**	**Complex I LYR protein (uncharacterized)**	**5.45**	**2**	**2**	**2**	**5.14**	**584**
200	**Q7SH52**	**Carbamoyl-phosphate synthase arg-3**	**4.43**	**1**	**1**	**1**	**1.71**	**1168**
201	**P06809**	**Cytochrome c oxidase subunit 4**	**4.27**	**1**	**1**	**1**	**8.60**	**186**
202	**P24919**	**Complex I, NDUFA5**	**4.03**	**1**	**1**	**1**	**6.59**	**273**
203	**A0A0B0DWW7**	**bL36m**	**4.01**	**1**	**1**	**1**	**11.29**	**124**

801